Lawrence Berkeley National Laboratory

Title
Strategies for gas production from oceanic Class 3 hydrate accumulations

Permalink
https://escholarship.org/uc/item/8k25q15k

Authors
Moridis, George J.
Reagan, Matthew T.

Publication Date
2007-05-01

Strategies for Gas Production From Oceanic Class 3 Hydrate Accumulations

George J. Moridis, SPE, LBNL
Matthew T. Reagan, LBNL

Abstract

Gas hydrates are solid crystalline compounds in which gas molecules are lodged within the lattices of ice crystals. Vast amounts of CH_4 are trapped in gas hydrates, and a significant effort has recently begun to evaluate hydrate deposits as a potential energy source. Class 3 hydrate deposits are characterized by an isolated Hydrate-Bearing Layer (HBL) that is not in contact with any hydrate-free zone of mobile fluids. The base of the HBL in Class 3 deposits may occur within or at the edge of the zone of thermodynamic hydrate stability.

In this numerical study of long-term gas production from typical representatives of unfractured Class 3 deposits, we determine that simple thermal stimulation appears to be a slow and inefficient production method. Electrical heating and warm water injection result in very low production rates (4 and 12 MSCFD, respectively) that are orders of magnitude lower than generally acceptable standards of commercial viability of gas production from oceanic reservoirs. However, production from depressurization-based dissociation based on a constant well pressure appears to be a promising approach even in deposits characterized by high hydrate saturations. This approach allows the production of very large volumes of hydrate-originating gas at high rates (> 15 MMSCFD, with a long-term average of about 8.1 MMSCFD for the reference case) for long times using conventional technology. Gas production from hydrates is accompanied by a significant production of water. However, unlike conventional gas reservoirs, the water production rate declines with time. The low salinity of the produced water may require care in its disposal.

Because of the overwhelming advantage of depressurization-based methods, the sensitivity analysis was not extended to thermal stimulation methods. The simulation results indicate that depressurization-induced gas production from oceanic Class 3 deposits increases (and the corresponding water-to-gas ratio decreases) with increasing hydrate temperature (which defines the hydrate stability), increasing intrinsic per-

meability of the HBL, and decreasing hydrate saturation— although depletion of the hydrate may complicate the picture in the latter case.

Introduction

Background. Gas hydrates are solid crystalline compounds in which gas molecules ("guests") occupy cavities within the lattices of ice crystals ("hosts"). Under suitable conditions of low temperature T and high pressure P, the hydration reaction of a gas G is described by the general equation:

$$G + N_H\, H_2O\ = G \bullet N_H\, H_2O \tag{1}$$

where N_H is the hydration number. Natural hydrates in geological systems usually contain hydrocarbons (for example, CH_4 and other alkanes), but may also contain CO_2, H_2S or N_2. Hydrate deposits occur in two distinctly different hydrogeologic settings: in the permafrost and in deep ocean sediments.

While no systematic effort has been made to map and evaluate the size of this resource (and current estimates vary widely, ranging between 10^{15} to 10^{18} m^3), the consensus is that the worldwide quantity of gas hydrates is vast. Gas hydrates are predicted to contain at least twice as much energy, even by the most conservative estimate, than all of the total known fossil fuel reserves recoverable by current methods. Thus, the attractiveness of hydrates, augmented by the environmental desirability of gas (as opposed to solid and liquid) fuels, is undeniable.

Classification of hydrate deposits. Natural hydrate accumulations are divided into three main classes.[6,7] Class 1 accumulations are composed of two layers: the Hydrate-Bearing Layer (HBL) and an underlying two-phase fluid zone with free (mobile) gas. In these deposits, the bottom of the hydrate stability zone (i.e., the location above which hydrates are stable because of thermodynamically favorable P and T conditions) coincides with the bottom of the hydrate interval. Production from Class 1 deposits is discussed in detail by *Moridis et al.*[7] Class 2 deposits consist of two layers: (1) an HBL, and (2) an underlying zone of mobile water (WZ). Class 3 accumulations are composed of a single hydrate interval (HBL), and have no underlying zone of mobile fluids. In Classes 2 and 3, the entire HBL may be well within the hydrate stability zone. A fourth classification, Class 4, pertains specifically to oceanic accumulations and refers to disperse, low-saturation hydrate deposits that lack confining geologic strata.[8]

Objective and Problem Description. The main objective of this study is to evaluate the production potential of Class 3

accumulations. Because of the bounded geometry of Class 3 hydrate deposits, an issue of particular importance is the selection of the appropriate method to induce the dissociation of hydrates.

Note that this study focuses on gas production from Class 3 accumulations that are bounded by confining upper and lower boundaries (referred to as the overburden and underburden, respectively). Class 3 accumulations without such near-impermeable boundaries are expected to have a lower gas production potential because of the lower pressure drops, gas losses through the overburden, and large water production volumes. Some earlier preliminary studies of gas production from Class 3 deposits have been reported,[9,10] but these did not benefit from recent advances in our understanding of the thermal and hydraulic behavior of hydrate-bearing geologic media.[11,12]

Dissociation Methods for Gas Production from Class 3 Hydrate Deposits

Gas can be produced from hydrates by inducing dissociation, which also releases large amounts of H_2O (Eq. 1). The three main methods of hydrate dissociation[13] are: (1) depressurization, in which the pressure P is lowered to a level lower than the hydration pressure P_e at the prevailing temperature T, (2) thermal stimulation, in which T is raised above the hydration temperature T_e at the prevailing P, and (3) the use of inhibitors (such as salts and alcohols), which causes a shift in the P_e-T_e equilibrium through competition with the hydrate for guest and host molecules.

Depressurization. While depressurization-induced dissociation, based on fluid removal through wells, appears to be the most promising strategy in gas production from Class 1 and Class 2 deposits,[7,14] the situation is far less clear in Class 3 accumulations because of the absence of a hydrate-free (and, consequently, relatively permeable) zone underneath the HBL from which fluids can be removed to induce depressurization of the overlying hydrates.

Thus, the attractiveness of depressurization--i.e., its simplicity, technical and economic effectiveness, and the fast response of hydrates to the rapidly propagating pressure disturbance--is challenged by permeability limitations in Class 3 deposits. In such deposits, the only method to induce dissociation by depressurization is via flow through the HBL. However, the low effective permeability $k_{eff} = k_{eff}(t)$ of the solid hydrate inhibits large flow rates, leading to low rates of dissociation and gas production, and a localized system response that is expected to be limited to the area around the production well.

Constant-Q depressurization. Thus, considering a cylindrical Class 3 deposit with a vertical well at its center producing at a constant mass rate Q_M, the corresponding volumetric gas production rate Q_P is

$$Q_P \propto A_D = 2\pi \Delta r_D h \qquad (2)$$

where A_D and Δr_D are the area and the width of the dissociation zone, respectively, and h is the thickness of the HBL. Conversely, depressurization-induced production from a Class 1 and Class 2 accumulations can be described as[7,14]

$$Q_{P12} \propto A_{D12} = 2\pi \Delta r_{D12} h + F_A \pi (r_{max}^2 - r_{D12}^2) \qquad (3)$$

where the subscript 12 denotes a Class 1 or Class 2 deposit, r_{D12} is the radius of dissociation around the well, r_{max} is the reservoir radius, and F_A is an area factor. As has been explained in other studies,[7,14] in Classes 1 and 2 the entire bottom base of the HBL begins dissociating in a uniform manner practically immediately upon the initiation of production ($F_A = 1$), and then a second dissociation interface develops at the top of the HBL ($1 < F_A \leq 2$). Comparison of Eqs. (2) and (3) reveals that, even at a very early stage (when $F_A = 1$), depressurization-induced gas production from Class 3 deposits under constant Q_M production appears to lag significantly behind that from Classes 1 and 2 ($Q_P << Q_{P12}$.). This is because the pressure disturbance cannot access the base or top of the HBL. This realization provides a potential insight into gas production from Class 3 hydrates: a plausible strategy to maximize Q_P would be to transform a Class 3 into Class 2 deposit through adoption of processes that enhance dissociation along the base of an HBL and development of an underlying water zone.

Increased hydrate saturation S_H is expected to progressively exacerbate the problem of low Q_P because of a reduction in k_{eff}. Additionally, if a high Q_M rate is imposed at the well and/or S_H is high in the HBL, ice can form because of the strongly endothermic nature of the hydrate dissociation reaction and Joule-Thompson cooling near the wellbore where gas velocities are high. Ice formation, especially when combined with secondary hydrate formation, can have a severe adverse effect on permeability, and can even result in cavitation[14] at the well. This is characterized by a drastic pressure drop to levels below the atmospheric that can lead to aqueous phase degassing and vaporization, and it may result in cessation of both fluid flow and gas production.

For the reasons discussed above, depressurization by imposing a constant Q_M at the well appears to be a possibility when (a) the intrinsic permeability k of the HBL formation is high, (b) the initial S_H is moderate (i.e., $S_H < 0.5$), (c) the capillary pressure P_{cap} is weak, and (d) the irreducible aqueous and gas saturations (S_{irA} and S_{irG}, respectively) are relatively low. Selection of this type of production presupposes knowledge that $k_{eff,0}$ (initial k_{eff}) of the HBL is capable of delivering the prescribed Q_M, and that the potential formation of secondary hydrate near the well[14] does not lead to $k_{eff} < k_{eff,0}$. Such knowledge may not be available *a priori*. Note that, while Q_M is constant, Q_P and Q_W (the water mass production rate) may vary over time as they depend on the transient phase mobilities.

Constant-P depressurization. Constant-pressure production involves the maintenance of a constant pressure P_w at the well, which acts as an internal boundary. The flow rates Q_M, Q_P and Q_W under constant-P production are not constant but vary over time because they are controlled by the time-dependent phase mobilities at the well and the pressure differential between the well and its surroundings.

Generally, it is not advisable to use constant-Q depressurization for gas production in Class 3 hydrate accumulations. This is because the k_{eff} of the formation can be very small (especially when $S_H > 0.6$), and as a result only very low constant rates can be applied over long times without cavitation.[9,10] Additionally, constant-Q production does not allow exploitation of a special feature of hydrate-bearing systems: that, un-

like conventional oil and gas systems, their k_{eff} increases over time as hydrate dissociates. Conversely, constant-P production is applicable to a wide range of formation permeabilities, is uniquely suited to allow continuous rate increases to match increasing permeability (the result of the dissociation-caused reduction in S_H), and may be the only reasonable alternative when S_H is high. An additional and very significant advantage of constant-P production is the elimination of the possibility of ice formation (with its detrimental effects on permeability and Q_P) through the selection of an appropriate P_w. This is ensured by selecting a $P_w > P_Q$, i.e., the P at the quadruple point $Q1$ (see Figure 1). Note that $P_Q = 2.6$ MPa for fresh water, but increases with salinity.[1,12]

A possible drawback is that constant-P production may lead to large initial Q_W, which, however, decreases over time. An additional potential drawback is that, by selecting a $P_w > P_Q$, both Q_P and the corresponding cumulative volume of produced gas V_P is reduced because the pressure differential $\Delta P = P_0 - P_w$ (the driving force of flow, dissociation and gas production) is not maximized. This is less of a problem in deeper and warmer oceanic accumulations, in which the initial pressure P_0 can be high, than in shallower oceanic accumulations and in the relatively shallow permafrost deposits. This complication can be resolved by (a) maximizing ΔP by selecting a P_w slightly above P_Q, and (b) varying P_w over time, keeping initially $P_w > P_Q$ until Q_P is significantly reduced (because of depressurization of the entire deposit) and then reducing P_w to levels below P_Q (and as low as the atmospheric). This is possible because, by the time P_w is reduced to below P_Q, S_H is expected to be sufficiently low as to either eliminate the possibility of ice formation upon continuing dissociation, or to limit the possible ice saturation S_I to levels which result in permeability reduction that is not prohibitive for gas production. Note that the final P_w, at which a considerable Q_P is observed, may be well below the normal abandonment pressure of conventional gas reservoirs.

Thermal stimulation. Earlier studies of gas production from Class 3 deposits[9,10] considered thermal stimulation to be the only viable alternative when S_H was high because of the low k_{eff} of such formations. However, thermal stimulation faces considerable challenges as a method for large-scale gas production from Class 3 deposits. The obvious shortcomings of the method include the very large energy requirements to raise the temperature of the subsurface, which has a large thermal inertia because of the high specific heat of (a) the geologic medium (remarkably uniform despite significantly different geochemical, mineralogical, hydraulic and textural properties), and (b) the inert (in terms of gas production) non-hydrate phases in the porous media (i.e., aqueous and gas). Note that the heat added to raise the temperature of phases other than the hydrate is essentially wasted, because it does not contribute to gas release. This is compounded by the inevitably increasing heat losses through the upper and lower boundaries. Considering the cylindrical HBL discussed earlier and heat addition through the vertical well, and assuming a sharp dissociation interface,[15] the heat losses are

$$H_L \propto 2\,\pi\,r_D^2 \qquad (4)$$

and increase rapidly with r_D. Thus, for a constant rate of heat addition Q_H, an ever increasing portion of the supplied heat is lost through the confining (but still thermally conductive) boundaries, while a continuously increasing fraction is needed to maintain the temperature gradient through the dissociated (hydrate free) zone from $r = r_w$ to the increasing r_D. This means that the Q_H fraction that reaches the hydrate and fuels dissociation is continuously shrinking, attesting to the inefficiency of the method.

The method of heat addition is important, and may exacerbate the inherently limited efficiency of thermal stimulation. If heat is added by the direct injection of warm fluids (almost exclusively water), this increases the aqueous saturation S_A and can create conditions adverse to the flow of the released gas to the well because of the reduction in the relative permeability for gas, k_{rG}. If the injected water is heated to some desired temperature T_w, the energy required may be prohibitively large because of the high specific heat of water. Warm brines (originating from deeper, warmer formations) appear to be a better alternative as injection fluids because they do not need heating and combine thermal stimulation with inhibitor effects that enhance hydrate dissociation. In this case, care must be taken to ensure that the salinity of the brines is such that their injection into the HBL does not lead to halite precipitation because of lower pressures, which could lead to a substantial reduction in permeability.

Direct water injection and use of the same well for both warm water injection and gas production leads inevitably to an adverse heat transfer regime because the released gas stream creates a low thermal conductivity k_Θ zone that reduces heat conduction to the hydrate front (advective heat transfer is limited because of the low k_{eff} of the main body of HBL). Additionally, the dissociation front is the locus of the highest pressures in the domain because of the released gas (Figure 2), resulting in flow stagnation as the countercurrent flows of gas (flowing from the dissociation front toward the well) and water (flowing from the injection point at the well toward the dissociation front) collide.[15] The warm injected water cannot come in direct contact with the dissociation front and efficiently exchange heat with it because of the escaping gas moving in the opposite direction, resulting in significantly reduced advective heat transfers. The resulting thermal regime involves heat addition to the dissociation process through slow conduction, with fast advective heat removal through the fluids produced at the well. Because of the different rates of these two heat exchange mechanisms, in addition to all the inefficiencies discussed previously, hydrate dissociation by means of thermal stimulation appears to be a self-limiting process.

An additional negative consequence of this method is that only a fraction of the released gas is produced. Since the dissociation front is the high-P ridge, gas moves toward the well (where it is collected) in addition to in the opposite direction, i.e., into the HBL and away from the well (Figure 2). The challenging thermal and flow regimes discussed above are a direct consequence of using the same well for both warm water injection and gas production. Significant improvements in gas production could be realized by using alternative well configurations that involve spatially separated gas production and water injection facilities.

A seemingly better method of thermal stimulation is direct heat application without fluid injection. Electrical or micro-wave heating (if possible) may have some advantages because they alleviate the competition between the injected warm water and the released gas and would not burden the relative permeability regime of the released gas stream. However, such heating may carry significant costs in terms of both special-ized equipment and heat production. A promising alternative is the use of fluids for heating without injection, e.g., using non-perforated pipes to circulate warm water along the well within the HBL. The main drawback of such an approach is that, in addition to the inherent heat losses, the transfer of heat to support hydrate dissociation is based on the slow conduc-tion, with a large fraction of the added heat lost through the fluids produced at the well.

Use of inhibitors. Although inhibitors can be very effective in promoting hydrate dissociation, their use for large-scale gas production from hydrates does not appear to be promising for several reasons. The dilution of the injected inhibitor stream by the large amounts of water released from dissociation (Eq. 1) continuously reduces their concentration and (conse-quently) their effectiveness. The injected aqueous stream car-rying the inhibitor faces mass transport challenges that are analogous to those of heat transfer (discussed in the case of thermal stimulation), and which limit the concentration of the inhibitor that comes in contact with the interface. Even when a continuous stream of full-strength inhibitor is available, flow stagnation at the dissociation front and dilution by fresh water release are certain to reduce its effectiveness. The problem can be further aggravated by (a) the cost of chemical inhibitors such as alcohols, and (b) the potentially adverse consequences of halite precipitation if salt-based inhibitors are used (e.g., warm brines).

Production potential and initial stability status. The pro-duction potential of a given hydrate deposit is determined by the following factors: (a) the method of inducing dissociation for production, (b) the intrinsic properties of the geological system, and (c) the initial stability of the hydrate, as described by the initial conditions. Of those, control can be exerted only on the production method, although the method itself is de-termined by the other two factors. Hydraulic properties are dominant in depressurization (flow-based) methods, and can exhibit significant spatial variability. Thermal properties are important in thermal stimulation methods, but are relatively uniform in the subsurface.

Hydrate stability is quantified by the distance between the initial P and T in the HBL (usually in the Lw-H region in Class 3 deposits, see Figure 1), and the corresponding location on the Lw-H-V line (i.e., the state of coexistence of aqueous, gas and hydrate phases, indicating dissociation). The closer the initial state is to the Lw-H-V line, the less stable the hy-drate will be, and the easier it will be to dissociate. Gas pro-duction from Class 3 hydrates involves moving the state of the HBL from its original position in the Lw-H region of the phase diagram (Figure 1) to an appropriate point on the Lw-H-V line.

The obvious corollary to this observation is that desirable targets for gas production involve deposits that are closest to the Lw-H-V line, because these are the easiest to destabilize and induce gas release. More stable deposits require higher depressurization and/or larger heat addition, and are obviously less desirable. For example, gas production from the Peru-Chile Trench 1 deposit[16] (P = 50 MPa and T = 6 ^{o}C) is almost impossible because of their high stability: the hydrate disso-ciation pressure P_e corresponding to T is 5.5 MPa, i.e., about $1/11^{th}$ of the actual P. Under these conditions, depressurization results in hydrate formation (as opposed to destruction) using the gas released from dissolution in the ocean water as the pressure drops.[8]

Among potential targets with initial conditions that are close to the Lw-H-V line, the more desirable ones are the ones with the highest initial T. This is because such deposits pro-vide a larger heat reservoir to fuel the endothermic hydrate dissociation reaction (and also preventing the early formation of ice), in addition to requiring a lower heat of dissociation. In marine deposits where the local geothermal gradient may vary significantly, this means that the deepest (and, consequently, warmest) hydrate deposits are the most desirable production targets as long as they are close to the Lw-H-V line. The same applies to permafrost deposits, although the maximum deposit depth is almost universal at about 1,200 m because of the much greater uniformity of the onshore geothermal gradient.

Geological System Description and Numerical Representation

The reference geologic system. The geologic system in this study was based on that of the Tigershark area[17] located in the Alaminos Canyon Block 818 of the Gulf of Mexico (Figure 3). Log data from an exploration well in about 2750 m (9000 ft) of water at the site indicated the presence of an 18.25-m (60-ft) thick sandy HBL (10,530 to 10,590 ft drilling depth) with a porosity ϕ of about 0.30 and Darcy-range intrinsic permeabil-ity.[17] Preliminary calculations[18] indicate that the S_H is in the 0.6-0.8 range, and that the base of the gas hydrate stability zone at this location occurs at or slightly below the base of the HBL.[17,18] Although the Tigershark deposit is a Class 2 de-posit,[14] its properties are particularly valuable in the study of a Class 3 deposit because they describe a promising target for gas production (as indicated by the high S_H and the thermody-namic proximity of the HBL to the Lw-H-V line in Figure 1), and because there are few other such data available.

Description of the modeled Class 3 hydrate deposits. The Class 3 deposit we investigated has the properties and initial conditions of the HBL in the Class 2 Tigershark reference deposit[14,17,18] (see Table 1), but has different boundary condi-tions. The Class 3 system has impermeable upper and lower boundaries (see Figure 4). The thickness of the overburden and the underburden were 30 m and 45 m respectively, which earlier calculations[7,19] had indicated to be sufficient to allow accurate heat exchange with the hydrate deposit during a 30-yr long production period (the expected life span of a well).

A cylindrical hydrate deposit is assumed (Figure 4), with a well placed at its center. As in the case of the Class 2 deposit investigated by *Moridis and Reagan*[14], the inner radius of the system was the well radius r_w = 0.1 m, its outer radius of was placed at r_{max} = 800 m (where a no-flow boundary of fluids and heat was located), and the well spacing was about 200 ha

(500 acres), with the no-flow boundary provided by the presence of other wells on the same spacing pattern. The hydraulic and thermal properties of the various formations in the domain under investigation (the HBL, the overburden and the underburden) are listed in Table 1. The relative permeability relationships that pertain to the porous media in the HBL and the corresponding parameters are based on data from the first field test of gas production from hydrates at the Mallik site,[5,15] while the P_{cap} relationships and parameters are consistent with the texture, porosity and permeability of the Tigershark formation.

The numerical simulation code. The numerical studies in this paper were conducted using the TOUGH+HYDRATE simulator, the successor to the earlier TOUGH-Fx/HYDRATE model.[12] This code can model the non-isothermal hydration reaction, phase behavior, and flow of fluids and heat under conditions typical of natural CH_4-hydrate deposits in complex geologic media. It includes both an equilibrium and a kinetic model[20,21] of hydrate formation and dissociation. The model accounts for heat and up to four mass components (water, CH_4, hydrate, and water-soluble inhibitors such as salts or alcohols) that are partitioned among four possible phases: gas phase, liquid phase, ice phase, and hydrate phase. A total of 15 states (phase combinations) can be described. The code can also handle any combination of hydrate dissociation mechanisms, phase changes, and steep solution surfaces that are typical of hydrate problems.

Simulation specifics

Domain discretization. Assuming equilibrium dissociation[23], the discretization of the cylindrical domain into 119 x 113 = 13,447 (r,z) gridblocks resulted in 53,788 coupled equations, and is identical to that used in the *Moridis and Reagan*[14] study of gas production from a Class 2 deposit at the Tigershark location. The identity of grids ensures a consistent geometric basis for the comparison of the gas production potential from the Class 2 and Class 3 deposits. The vertical discretization in the HBL was very fine ($\Delta z = 0.25$ m), and the radial discretization includes a very fine grid in the all-important vicinity of the wellbore (especially in the $r < 20$ m zone) that controls production from the entire deposit.[14] Interested readers are directed to the study by *Moridis and Reagan*[14] for a detailed discussion of the domain discretization, in addition to a thorough description of the initialization process.

Initial conditions. A pure CH_4-hydrate is assumed. The initial conditions in the HBL are identical to those in the HBL of the companion Class 2 study.[14] An additional reason for using the same grid is to avoid repeating the laborious initialization process of gravity equilibration that a different grid would require.

Well description. In describing the well, flow through the wellbore is represented using the pseudoporous-medium approach of *Moridis and Reagan*.[14] Under constant-Q production, Q_M is assigned to the topmost gridblock describing the wellbore, and the contributions of the various gridblocks in contact with the wellbore is determined from the relative mobilities. For constant-P production, the topmost gridblock in the subdomain representing the wellbore is treated as an internal boundary that was maintained at the constant bottomhole pressure P_w.

Simulation process and outputs. The maximum simulation period is 30 years (corresponding to the typical life span of a well), but the deposit was either exhausted earlier or the simulation was interrupted when Q_P was shown to remain at low (and commercially unattractive) levels over periods that were sufficiently long to preclude any further consideration of the production method under consideration. In the course of the simulation, the following conditions and parameters are monitored: spatial distributions of (a) P, (b) T, (c) S_H and S_G, and (d) water salinity, expressed as the mass fraction of salt X_i in the aqueous phase; volumetric rate of CH_4 released from dissociation and of CH_4 production at the well (Q_R and Q_P, respectively); cumulative volume of CH_4 released from dissociation and of CH_4 produced at the well (V_R and V_P, respectively); and water mass production rate at the well (Q_W) and cumulative water mass produced at the well (M_W).

Production cases. We investigated three cases involving different dissociation-inducing production methods. Of those, the first two cases were based on thermal stimulation, and third case employed only constant-P depressurization. In all three cases, the production (perforated) interval covered the entire thickness of the HBL, and Q_P and Q_W were determined from the corresponding phase mobilities at the well contact with the formation. Because of the need to satisfy the irreducible gas saturation, S_{irG}, requirement for flow to occur after the initial gas release from dissociation, gas production at the well was expected to lag behind gas release into the deposit and water production. The three cases we investigated are as follows:

Case A: Thermal stimulation by circulating warm ocean water in the well. In Case A, warm ocean water with $X_i = 0.03$ (the most likely injection fluid in an oceanic operation) was circulated in the well. This is similar in design and operational parameters to the method used to induce dissociation in the Mallik field test of gas production from a permafrost deposit.[5,15] Thus, in this study, this method combines two dissociation mechanisms: thermal stimulation and use of an inhibitor.

To numerically describe the process and effects of water circulation, warm water was injected into the gridblock corresponding to the bottom of the wellbore at a rate of $Q_I = 6$ kg/s (0.35 m^3/min), which was the rate used in the Mallik test[5,15]. Water and gas were produced at the same rate from the uppermost gridblock of the wellbore. This configuration provided the numerical equivalent of warm water circulation at the well. The specific enthalpy of the circulated warm water was $H_W = 2.75 \times 10^5$ J/kg (corresponding to a temperature of about 62 °C at the injection pressure). The source of such water could be either a deeper, warmer geologic formation, or heated ocean water. The circulation pattern provides a mild pressure gradient across the well.

The warm saline water is expected to supply heat to the formation through conduction and advection. Heat transfer and gas relative permeability are challenged by the processes discussed earlier. The released gas is expected to hug the dissociating interface, rise to the top of the HBL because of buoyancy, and escape to the low-pressure collection point at the top of the wellbore. Secondary hydrate formation is not

expected around the wellbore in this thermal stimulation case, but it is expected behind the dissociation front (the locus of the maximum P in the domain) as some of the released gas moves away from the dissociation front and into the main body of the hydrate. This production method is based on a very simple design, involves conventional technology, and poses no particular technical challenges.

Case B: Thermal stimulation by electrical heating. While the entire length of the wellbore is still perforated in Case B as in Case A, its outer surface is equipped with electrical heating coils that can provide heat at a constant rate $Q_H = 600$ W/m that is uniform along the wellbore. This is similar to the rates used in exploratory studies of the design of the Mallik test.[9] The gridblock above the uppermost gridblock of the wellbore subdomain was kept at a constant pressure equal to the hydrostatic pressure at this elevation (the initial P at the well). The pressure differential necessary for flow to the well would be provided by density differences and the resulting convection cells (e.g., buoyancy of the gas, and buoyancy of the heated, less saline water from dissociation) in addition to the higher pressure along the dissociation front caused by the gas release. As in Case A, the locus of any secondary hydrate was not expected to be around the well, but instead behind the dissociation front.

The well design in Case B is more complex that in Case A, and may involve technology that is not standard in oil and gas production, but does not pose any insurmountable technical problems.

Case C: Constant-P depressurization. Case C involves a simple well design that employs a constant bottomhole pressure. This is described by an internal boundary located in a gridblock above the uppermost gridblock in the well subdomain. By imposing a constant bottomhole pressure P_w and a realistic (though unimportant) constant temperature T_w at this internal boundary, the correct constant-P condition was applied to the well while avoiding any non-physical temperature distributions in the well itself (the large advective flows into the well internal boundary from its immediate neighbor eliminated any potential heat reverse heat transfer effects that could have resulted from an incorrect T_w). The initial bottomhole constant $P_w = 3$ MPa is greater than P_Q, thus eliminating the possibility of ice formation and the corresponding potentially dramatic effect on k_{eff}. At a later stage ($t = 5,000$ days), P_w could be safely reduced to $P_w = 0.5$ MPa $< P_Q$ to increase the driving force of flow, ΔP, and thus maximize Q_P and V_P, without the possibility of ice formation because the hydrate has already been exhausted.

Because of the well configuration in Case C, secondary hydrate could form next to the wellbore due to cooling from the endothermic hydrate dissociation reaction as well as the Joule-Thompson phenomenon (which is at its maximum in the immediate vicinity of the well, where the highest gas flow velocities occur). As in Case A, this production method is based on a very simple design, involves conventional technology, and poses no particular technical challenges.

System Response During Production in Case A

Evolution of gas and water releases. Figure 5 shows the evolution of the volumetric rates Q_R and Q_P of CH_4 release and production at the well. respectively. in Case A. Gas re-

lease begins almost immediately upon contact of the hydrate with the warm water, and gas production follows shortly thereafter. As expected, Q_R consistently exceeds Q_P because of the need for gas accumulation in the reservoir until the gas saturation overcomes its irreducible level and production can begin. Initially, both Q_R and Q_P increase rapidly because of the large early rates of heat arrivals at the dissociation front. These initial high heat rates are made possible by the large initial temperature differential between the wellbore and the undisturbed hydrate beyond the wellbore, in addition to the increasing advection of the warm ocean water into the HBL. However, the net heat arriving at the dissociation front begins to decrease as the dissociation front recedes (thus making advection more difficult given the absence of injection) and the temperature differential (the driving force of advection) between to the wellbore and its surroundings declines. Because of this, in addition to the increasing heat losses and the increasing difficulty in heat transfer (as discussed in an earlier section), Q_R and Q_P begin to decline continuously after peaking at about $t = 400$ days. Q_P is further hampered by an adverse k_{rG} regime as the released gas moves toward the collection point at the well against the invading circulation water.

The most important observation from Figure 5 is the low level of Q_P, which never exceeds 5.2×10^{-3} ST m^3/s (16 MSCFD) of CH_4. This is orders of magnitude lower than the 2-6 ST m^3/s (6-18 MMSCFD) that can be attained from a Class 2 formation[14] with the same HBL characteristics as in this Class 3 study. Such low production led earlier studies[9,10] to the conclusion that Class 3 deposits have low potential and are consequently undesirable production targets. These conclusions were erroneous because the low production is a result of the inadequacy of thermal dissociation methods alone, rather than a systemic shortcoming of Class 3 hydrate deposits. As will become apparent later in this study, alternative production strategies show greater promise.

Because Q_P remains low, declining after $t = 400$ days, and consistently far below levels that are considered economically viable in offshore systems (usually several MMSCFD), the simulation was interrupted after $t = 1,840$ days because there was no physical reason for a possible major surge in production after that time. Even if such a possibility existed, it is unlikely that any commercial operation can sustain a 5-year period of minuscule production in the hope of a more rewarding future.

Figure 5 also shows Q_P when fresh (instead of ocean) water is circulated in the well, and provides a measure of the effect of the inhibitor on dissociation. Although Q_P is larger for ocean water circulation, the difference is small and is consistent with expectations (see earlier discussion) because of the dilution of the saline water by the fresh water released from hydrate dissociation.

The Q_W rate in Figure 6 is practically constant during the simulation period, resulting in the nearly linear shape of the M_W curve. The gradual decrease in Q_P (after an initial surge) while Q_W remains constant is attributed to the increasing heat losses and heat transfer challenges, which reduce the heat arriving at the dissociation front. Additionally, an increased fraction of the released gas is stored in the reservoir to satisfy the $S_G > S_{irG}$ condition for the initiation of flow to the well.

Spatial distributions of S_H and S_G. In all of the figures that describe the spatial distribution of reservoir properties and conditions in Cases A through C, the initial position of the HBL extended between the $z = -30$ m datum and the y-axis line at $z = -48.25$ m. Comparison of the hydrate distribution to the initial HBL extent provides a measure of the magnitude of dissociation of the hydrate.

Figures 7 and 8 show the evolution of the S_H and S_G distributions over time in the deposit near the wellbore ($r < 40$ m) at two different times, $t = 280$ days and $t = 1840$ days (end of simulation). The most obvious observation from these two figures is the limited extent of hydrate dissociation over this period, and the rather uniform dissociation pattern. The warm water invading the bottom of the HBL results in more intense dissociation at that location, reaching deeper into the formation. The flow of gas from the dissociation front into the HBL results in the formation of secondary hydrate, depicted by a higher S_H behind the dissociation front in Figure 7. Note that the maximum S_H is observed in a thin zone near the top of the formation and at some distance from the dissociation front. Because of buoyancy, the released gas is expected to move to the top of the HBL, where it can form additional hydrate at a location where T is still unaffected. As time advances, the initial sharp dissociation front in Figure 7a becomes a wider and more diffuse dissociation zone, as seen in Figure 7b.

The S_G distribution in Figure 8a indicates that gas released from hydrate dissociation hugs the interface and rises in contact with it, reaching the top of the HBL and then escaping at the well. As time advances and the dissociation front recedes from the well, a gas bank is established below the base of the underburden (Figure 8b). This is caused by gas buoyancy, and acts as a gas source feeding the well. Because the warm water invading from the well cannot penetrate deep into the HBL, the width of the gas zone increases over time (Figure 8b). Because of the width of the S_G zone and the very low k_Θ of the gas, the thermal conductivity of the area immediately in front of the dissociation front (and the corresponding heat transfer) is significantly reduced, while the direction of flow of CH_4 away from the front impedes advective heat transfer.

Spatial distributions of T. The T distribution in Figure 9 provides a description of the invasion pattern of the injected water. Note the limited warm water incursion even after 5 years of production (Figure 9b). The expanding temperature disturbance at the top and bottom of the HBL indicates the ever-increasing area over which heat losses occur.

Spatial distribution of X_i. The distribution of the salt concentration (expressed as the mass fraction of salt, X_i, in the aqueous phase) in Figure 10 shows the dilution effect of dissociation on salinity. The ocean water circulating at the well is at its maximum X_i level, but is diluted when it enters the HBL and mixes with fresh water produced during hydrate dissociation. The maximum dilution occurs at the location of maximum dissociation, i.e., along the dissociation front and initially concentrated close to the HBL base (Figure 10a). As time advances, the thermal front expands (see Figure 9b), while warm water rises because of buoyancy and lower density (Figure 10b). Dissociation, mixing and dilution of the invading and native waters with the fresh water from dissocia-

tion leads to the formation of a zone of low salinity that begins at the bottom, is in contact with the dissociation front, and is expelled at the well.

System Response During Production in Case B

Evolution of gas and water releases. Figure 11 shows the evolution of the volumetric rates Q_R and Q_P of CH_4 release and production at the well, respectively, in Case B. As discussed earlier, this is different scenario than that discussed in Case A as it involves the application of heat without fluid injection. The differences are reflected in the drastically different appearance of the Q_R and Q_P curves, compared to those in Figures 5 and 6 (Case A). Both Q_R and Q_P exhibit a periodic (sinusoidal) appearance with a downward trend. This is caused by the manner of dissociation and the pattern of flow. Because the top of the well is maintained at a constant hydrostatic pressure (equal to its initial pressure), the pressure differentials that drive flow are much smaller and arise from pressure increases caused by gas evolution at the dissociation interface and buoyancy and convection close to the heated wellbore. As heat arrives at the dissociation front, dissociation occurs. This has a dual retardation effect on further dissociation: by increasing the P and decreasing the T (albeit locally), the rate of dissociation decreases, and can be resumed at close to its initial rate only after enough time has elapsed to allow the slow conduction process (the main heat transfer mechanism) to supply more heat to the dissociation front (the higher P at the front restricts or eliminates advective heat flows). This results in the periodic appearance of Figure 11, a physical phenomenon that is further exacerbated by numerical discretization issues.

Gas release begins almost immediately upon contact of the hydrate with the heated water, and gas production follows shortly thereafter. Q_P is at its maximum very early, i.e., at the time of the largest temperature differential between the wellbore and the undisturbed hydrate beyond the wellbore. As time advances, the oscillations become progressively more attenuated because of the smoother and milder temperature gradient. The declining trend is caused by the continuously increasing heat losses through the boundaries.

As expected, Q_R consistently exceeds Q_P because gas saturation must first reach its irreducible level before production can begin. Initially, both Q_R and Q_P reach an early maximum because of large amount of heat provided to the newly formed dissociation front. An additional reason for the sinusoidal appearance of the Q_P curve is that pressure gradually builds up as gas accumulates in the reservoir prior to its release when $S_G > S_{irG}$. In each production cycle, pressure drops when gas reaches the well and is produced. Scrutiny of the Q_R and Q_P curves indicates a phase shift, with Q_R being at its minimum (indicating maximum P and gas accumulation) when Q_P is at its maximum (favored by the same conditions, and fueled by the larger ΔP). Although the phase shift is initially 90°, it begins to decrease with time as the dissociation front moves deeper into the HBL, the thermal gradients become milder, and the distance that gas has to cover before discharge increases.

Notwithstanding the oscillations, Q_P in case B is very low and continuously decreasing over time (albeit very slowly), with a maximum of about $Q_P = 1.6 \times 10^{-3}$ ST m^3/s (5 MSCFD)

of CH$_4$. This is much lower than in Case A (Figure 5), and orders of magnitude lower than the 2-6 ST m^3/s (6-18 MMSCFD) that can be attained from a Class 2 formation[14] with the same HBL characteristics. The reason for the absence of the initial Q_P surge (as observed in Case A, see Figure 5) is the lack of the very effective advective heating. Because of the low and continuously declining Q_P, the simulation was interrupted after t = 3,780 days, i.e., before the exhaustion of the hydrate.

The Q_W rate in Figure 12 shows a relatively large initial water release that decreases continuously until t = 1,000 days. After that time, Q_W oscillates about a roughly constant mean. The larger initial Q_W rates are attributed to the larger initial permeability of water when S_G is low, which leads to preferential water expulsion as pressure increases. As time advances and S_G increases, the mobility of H$_2$O decreases, leading to progressively lower Q_W. The system eventually reaches a quasi-steady state after t = 1,000 days, during which the amount of heat reaching the dissociation front is almost constant (i.e., the decline is very slow), and both Q_P and Q_W stabilize with a slight downward trend.

Thus, Q_P in Case B is extremely low (even lower than the unacceptably low production in case A), and cannot satisfy minimum economic viability conditions under any circumstances.

Spatial distributions of S_H and S_G. Figures 13 and 14 show the evolution of the S_H and S_G distributions over time in the deposit near the wellbore ($r < 40$ m) at two different times, t = 327 days and t = 3780 days (end of simulation). As in Case A (Figure 7), the most obvious observation from these two figures is the limited extent of hydrate dissociation over this period, and the rather uniform dissociation pattern. This was expected, given the magnitude of Q_R in Figure 11. Unlike Case A, the S_H pattern shows more intense hydrate destruction pattern near the top of the HBL. This is caused by buoyancy, which brings the warmer, less saline, and thus less dense water that first evolves at the bottom (where dissociation is easier due to higher initial temperature) to the top of the HBL through convection. The flow of gas from the dissociation front into the HBL results in the formation of secondary hydrate, depicted by a higher S_H behind the dissociation front in Figure 13. As in Case A, the maximum S_H is observed in a thin zone near the top of the formation and at some distance from the dissociation front (Figure 13b). Because of buoyancy, the released gas is again expected to move to the top of the HBL, where it can form additional hydrate at a location away from the dissociation front and where T is still unaffected by heating. As time advances, the initial sharp dissociation front in Figure 13a becomes the wider and diffuse dissociation zone in Figure 13b.

Because of the S_H distribution (inverted with respect to case A), the S_G distribution in Figure 14a indicates gas rising to the top of the formation, where it accumulates in the space provided at the top of the HBL before flowing to the well. As time advances and the dissociation front recedes from the well, a gas bank is established below the base of the underburden (Figure 14b), and the previous pattern is amplified. This is caused by gas buoyancy, and acts as a gas source feeding the well. Because there is no fluid invading the HBL from the

well, the width of the gas zone increases over time (Figure 14b). Because of the width of the S_G zone and the very low k_Θ of the gas, the thermal conductivity of the area immediately in front of the dissociation front (and the corresponding heat transfer) is significantly reduced.

Spatial distributions of T. The T distribution in Figure 15 provides an illustration of the convective thermal flows caused by the application of heat. Note the limited reach of the thermally affected zone even after over 10 years of production (Figure 15b). The expanding temperature disturbance at the top and bottom of the HBL indicates the temporally ever-increasing area over which heat losses occur.

Spatial distribution of X_i. The distribution of the salt concentration (expressed as the mass fraction of salt X_i in the aqueous phase) in Figure 16 shows the dilution effect of dissociation on salinity, in addition to the effect of water removal during production. The water released from dissociation continuously dilutes the native water in the HBL, while the produced water is being replenished with the fresher water released from hydrate dissociation. Because of buoyancy of the lighter, fresher water and drainage of the heavier, more saline water, fresh water accumulates near the top of the HBL. As time advances, the thermal front expands (see Figure 15b), as does the zone of reduced salinity immediately ahead of the dissociation front (Figure 16b). As in Case A (Figure 10), the band of the lowest-salinity water is located in contact with the dissociation front.

System Response During Production in Case C

Evolution of gas and water releases. Figure 17 shows the evolution of the volumetric rates Q_R and Q_P in Case C. The differences between Figure 17 and the corresponding figures for cases A and B (Figures 5 and 11) could not be more dramatic. The patterns of both Q_R and Q_P are characterized by a series of cyclical (oscillating) events. The constant-P depressurization results in an initial "burst" of gas release as the hydrate in the immediate vicinity of the well dissociates very rapidly. After this initial (and very short) explosive release stage, Q_R begins to increase quickly as hydrate saturation near the wellbore decreases through hydrate dissociation, increasing k_{eff}. The initial increasing trend is followed by a sharp decline in Q_R. As time progresses, each production cycle consists of a long stage of increasing Q_R, followed by a short stage of sharp decline. Q_P exhibits the same pattern. Additionally, the temporally local maxima and minima of Q_R and Q_P occur at the same times. The pattern is repeated until the cessation of production when Q_P = 0.3 ST m^3/s of CH$_4$ (1 MMSCFD) at t = 6,000 days.

Q_P in constant-P production begins in earnest from the moment depressurization is applied. This is in stark contrast to of production from Class 2 deposits with the same initial conditions[14], which is characterized by long lead times (about 550 days) of low production (Q_P = 0.2 ST m^3/s of CH$_4$ = 0.6 MMSCFD). Thus, from very early on, Q_P in constant-P production from Class 3 deposits reaches very high levels, with cycle maxima that regularly exceed 5 ST m^3/s of CH$_4$ (15 MMSCFD). The startling realization from Figure 17 is that Class 3 hydrate deposits have a gas production potential that is

as good as that of Class 2 deposits, and are even more desirable at he early stages of production. As indicated earlier, P_w is decreased from 3 MPa to 0.5 MPa at about t = 4,900 days. This occurs after the exhaustion of hydrate through dissociation at t = 4,800 days, which is marked by Q_R = 0. Upon production with a lower P_w, a surge in Q_P is observed. Because of gas stored in the reservoir, Q_P continues for over 1,000 days after the depletion of the hydrate. Figure 17 also shows the average gas production Q_{avg} = 2.61 ST m^3/s (8.10 MMSCFD) during the 6000-day production period.

Note that quite often during the production pattern in Figure 17, Q_P exceeds Q_R, indicating that gas production is partially supported by the gas stored in the reservoir from earlier releases. This is evident in Figure 18, which shows the cumulative volumes V_R and V_P for Case C. V_R consistently exceeds V_P, indicating continuous storage of extra released gas. As Figure 18 shows, at the end of the 6000-day simulation period, a total of V_P = 1.37x10^9 ST m^3 (4.84x10^{10} ST ft^3) have been produced, all of which originated from the hydrate. This corresponds to a 99% recovery of the gas initially stored in the hydrate deposit.

Figure 19 shows the water mass production rate Q_W at the well and the corresponding cumulative mass of produced water M_W. Despite the oscillations in each production cycle, the overall pattern shows an exponential-like decline of Q_W from a large initial level to a roughly constant level, before the switch to the lower P_w. At its peak immediately upon the initiation of production, Q_W = 23 kg/s (12,200 BPD), but it declines quickly to an average of about Q_W = 2.5 kg/s (1,300 BPD) after t = 1,000 days. Even at its highest, Q_W is manageable, as is the cumulative mass of produced water M_W. Note that production from Class 3 hydrates by constant-P depressurization is at its most challenging upon initiation, and the picture continuously improves with time. This is the exact opposite of what happens in production from conventional gas reservoirs, and appears to be a significant advantage as it dictates planning for the worst-case scenario at the beginning rather toward the end of production.

The results in Figures 17 to 19 demonstrate the clear superiority of the production method in Case C over those in Cases A and B. Additionally, they clearly indicate that there is nothing intrinsically prohibitive in the production from Class 3 hydrates, and provide convincing evidence that the earlier impressions of low production potential of such hydrate deposits[9,10] were the result of inappropriate production methods.

Spatial distributions. Figures 20 and 21 show the evolution of the S_H and S_G spatial distributions over time within the critical narrow zone (r < 18 m) around the wellbore (see the similar discussion in *Moridis and Reagan*[14]). These figures provide an explanation for the cyclical pattern of Q_R and Q_P observed in Figure 17. The precipitous drop in Q_R and Q_P is caused by the appearance of the *traveling dual barrier* that is formed from secondary hydrate around the well (Figure 20). This feature has not been encountered before, and appears to be inextricably connected to the constant-P depressurization process. As dissociation proceeds and gas flows to the well, the conditions around the wellbore promote the formation of a secondary hydrate barrier next to the wellbore (Figure 20a). This is further promoted by the dilution of the water salinity

(Figure 22a). Because of inner radius of the cylindrical barrier is exposed to intense depressurization, it dissociates, but additional hydrate is accumulated on its outer radius. This results in the barrier moving away from the well (Figure 20a), giving the appearance of a traveling barrier.

The flow restriction and the intense dissociation within the cylindrical chamber in Figure 20b leads to low temperature (see Figure 23a to 23c) that are below the hydration temperature T_e at the prevailing P within the chamber. This leads to the formation of a second barrier (Figure 20c) that is initially close to the wellbore, and then moves away through the previously described process. Note that the emergence of such secondary hydrate barriers can occur within a very short time (no longer than a few hours) when the appropriate P and T evolve. The barrier closer to the wellbore becomes now the main barrier to flow, with intense depressurization in front of it (Figures 24b to 24d) with gas flowing unencumbered over the top and around the outer barrier (Figure 21c and 21d). Under these conditions, the outer barrier is no longer exposed to depressurization (Figure 24d), while exposed to the warmer temperature of the slower moving fluid behind it (Figure 23d). This leads to the outer barrier dissociation because of the rising temperature (Figures 20d and 23d, and is attested to by the X_i distribution in Figure 22d) which shows only declining salinity at the location of the outer barrier. Conversely, barrier formation is indicated by higher salinity as the hydrate crystal expels salt. This is clearly demonstrated by the X_i distribution during the formation of the inner barrier in Figures 22b to 22d.

Figure 20e shows the S_H distribution after the inner barrier of Figure 20d has begun to decompose, and another inner barrier has formed. This inner barrier of secondary hydrate is depicted by the X_i distribution in Figure 22e, as well by the low T in the inner chamber (Figure 23e), and the low corresponding P (Figure 24e), which is expected to induce dissociation of the inner surface of the inner radius. After the complete depletion of the outer barrier of Figure 20e (see Figure 20f), the remaining single barrier has moved away from the well. During all these times, gas continues to accumulate at the top of the HBL because of buoyancy, while flowing over, through and below the barriers toward the well (Figures 21b to 21f).

The pattern is repeated again in Figure 20g, which shows the formation of yet another inner barrier and the continuing destruction of the outer barrier (the one in Figure 20f). The hydrate formation in Figure 20g is confirmed by the X_i signature in Figure 22g (that shows a salinity increase at the location of the barrier), in addition to the low T and depressurization seen in Figures 23g and 24g, respectively. Note the pressure buildup behind the barrier in Figure 24g (as compared to the earlier distribution in Figure 24f) that is effective because of more complete flow restriction with this incarnation of the secondary hydrate barrier. Gas is shown to dip under the lower tip of the barrier and then curve upward to reach the well (Figure 21g).

This pattern continues until the end of production. As time advances, the traveling dual barrier continues to appear and disappear (Figures 20h to 20k), the pressure generally drops, although build-up may be observed if an inner barrier is relatively impermeable (Figures 24h-k), if gas flows to the well while accumulating at the top of the HBL (Figures 21h-k), and

if the system becomes progressively cooler and less saline (Figures 23h-k, and 24h-k).

Each of the precipitous Q_R and Q_P drops in Figure 17 occurs when the inner secondary hydrate barrier is formed and the traveling outer barrier is in place. Note the accumulation of gas at the base of the overburden, a feature typical to all hydrate deposits produced by depressurization,[7,14] along with the development of a second dissociation interface at the top of the HBL. This is clearly shown in Figure 25, which exhibits the reservoir-scale S_H distributions at different times for Case C. The gas accumulation pattern has particularly important (and potentially severe) implications for gas production from oceanic Class 3 (in addition to Class 2)[14] deposits because lack of a confining overburden could lead to gas loss through percolation though the overburden and release at the ocean floor.

Figure 25 also shows very uniform dissociation patterns along the entire reservoir radius r_{max}. Although the reservoir-scale distribution of S_G in Figure 26 is not as uniform, nevertheless its distribution and variation are smooth. The obvious conclusion is that, as in Class 2 deposits, Class 3 hydrate deposits under depressurization-induced production dissociate uniformly along the entire area of their horizontal interfaces, a behavior that is caused by the very large effective permeability disparity between the HBL and its hydrate-free surroundings. This finding supports the realization made in the study of Class 2 hydrates: that processes and phenomena that occur within a narrow zone around the well control gas production from the entire hydrate deposit.[14] As in Class 2 deposits, this critical zone has a radius $r_c < 15$-20 m (see Figure 20), and fine discretization must be used for its simulation if these near-well phenomena are to be captured and accurately described.[14]

Sensitivity Analysis

Because of the overwhelming advantage of the underlying depressurization-based production method, the sensitivity analysis focused on in Case C. We investigated the sensitivity of gas production to the following conditions and parameters:

    (a) The stability of the hydrate deposit, as quantified by its temperature T and its deviation from the equilibrium temperature at the prevailing pressure,

    (b) The initial hydrate saturation S_{H0},

    (c) The intrinsic permeability k.

Sensitivity to T. Compared to the reference case, a colder and more stable hydrate deposit is expected to exhibit slower gas emergence, and to have a lower Q_P and V_P, in addition to a lower M_W. This is because (a) the increased stability requires a larger depressurization for the evolution of gas, (b) because of the lower temperature, the fraction of depressurization fueling dissociation is limited, and consequently, the driving force fueling dissociation is diminished, and (c) the reduced rate of dissociation does not lead to a rapid increase in the effective permeability of the hydrate-bearing formation, thus limiting the rate of water release. Figure 27a shows the strong dependence of Q_P on the hydrate stability, as quantified by the system temperature T (in this case lowered by 10 °C over that in the reference Case C, see Table 1) at a given pressure. The results in Figure 27a conform to the expectations, and indicate a Q_P that is only a fraction of that for the reference case.

For the reasons already discussed, the corresponding V_P and M_W in Figures 28a and 28b, respectively, are substantially lower than those in the reference case (included in Figure 28). Although the information in Figures 27 and 28 is useful, an additional variable is necessary for a thorough evaluation of the production potential of such hydrate deposits. Thus, the appeal of a production approach (in terms of technical feasibility, gas production potential and economic viability) is evaluated by employing two criteria: an absolute criterion of sufficiently high gas production, and a relative criterion of an acceptably low water-to-gas ratio. The former may not be fully satisfied by the relative low production rates and volumes shown in Figures 27 and 28. The latter is defined as $R_{WGC} = M_W/V_P$, involves cumulative quantities that describe the performance over the duration of production, and provides a measure of water production per unit standard volume of produced gas that can be used for technical and economic feasibility evaluation.

The evolution of R_{WGC} in Figure 29 indicates that the water-to-gas ratio is high over a short initial period, but it rapidly (and continuously) improves as time advances. The consistently higher (than that for the reference case) R_{WGC} describes the much larger water production in more stable systems, demonstrates the importance of temperature as a selection criterion of a hydrate deposit as a production target, and indicates the relative undesirability of stable hydrates as an energy resource. For a given pressure, the attractiveness of such deposits increases with T, and with the proximity of T to the equilibrium temperature. Note that Figure 29 shows that the reference Case C appears to have the most desirable R_{WGC} performance from among the various perturbations.

Sensitivity to $S_{H,0}$. Figure 27a shows the dependence of Q_P on $S_{H,0}$. A lower $S_{H,0}$ leads to a higher Q_P because of the larger effective initial permeability to water, and, consequently, the faster depressurization and hydrate dissociation. Thus, during the early stages of production, Q_P is larger when $S_{H,0} = 0.5$ than in the reference case, in which $S_{H,0} = 0.7$ (Table 1), and largest when $S_{H,0} = 0.3$. This is further indicated by the earlier and higher Q_P peaks (Figure 27a). Because of the oscillating nature of the Q_P curve, it is not possible to draw conclusions about gas prodution at later times. For this, we have to rely on the V_P curve.

The cumulative V_P and M_W in Figure 28 show a strong dependence on $S_{H,0}$. The largest V_P and M_W in Figure 28 are observed for the $S_{H,0}$ perturbations. This is not an unexpected result, given the complete dependence of depressurization-based techniques on flow and the larger effective permeability of low-$S_{H,0}$ systems. Figure 28a shows that the improvement in V_P with a decreasing $S_{H,0}$ is not monotonic because the increasing leanness of the resource eventually begins to adversely affect V_P. Thus, although V_P for $S_{H,0} = 0.3$ initially exceeds that for $S_{H,0} = 0.5$, the relationship is later reversed because of the exhaustion of the limited hydrate resource. Because of the increased effective permeability of water in the low-$S_{H,0}$ system, the corresponding M_W increases with a decreasing $S_{H,0}$ (Figure 28b)

The evolution of R_{WGC} in Figure 29 confirms this observation. Thus, the larger initial water saturation and the correspondingly larger effective permeability overwhelm the larger

gas production associated with the leaner hydrate systems and lead to a R_{WGC} that increases with a decreasing $S_{H,0}$ and is higher than that for the reference Case C.

Sensitivity to *k*. A reduction of k to 50% and 10% of its reference value (Table 1) results in commensurate reductions in Q_P (Figure 27b), V_P (Figure 28a) and M_W (Figure 28b) closely follows that in the reference case for reasons already explained. This was expected because of the exclusive reliance on flow (and the underlying permeability) for this type of depressurization-based dissociation, and the k-affected adverse gas flow regime can be particularly challenging immediately after the gas release and the beginning of the gas flow. An interesting observation is that the effect of k is roughly linear. This is in contrast to production From Class 2 deposits, in which the effect is sublinear[14].

The resulting R_{WGC} in Figure 29 integrates these ideas, indicating that, (a) while the initial water-to-gas ratio decreases with a decreasing k and is lower than that in the reference case because of the k-related impedence to flow, (b) the long-term improvement that is typical of all such Class 3 systems does not materialize, with the long-term R_{WGC} deteriorating with a decreasing k. Thus, the two worst long-term R_{WGC} cases in Figure 29 correspond to the two low-permeability studies. This indicates that the difficulty of the development of a free gas phase and the establishment of long-term gas flow are progressively more difficult in low-k systems, in which water flow has an increasing advantage. The obvious conclusion is that more permeable systems are better production candidates because of both a higher V_P and a lower R_{WGC}.

Of particular interest is the evolution of the S_H distribution in the deposit in the $k = 0.1$ k_{ref} case (Figure 3). While the traveling barriers discussed in the analysis of Figure 20 are observed in this low-k case, what is significantly different is that the barrier that is farthest from the well does not begin to "atrophy" and disintegrate once it reaches its final position (as happens in the reference case), but instead remains at its position practically unaffected. The next traveling barrier arrives at the same position, and the two collide and fuse. The process continues, and each emerging new barrier (the evolution of which is marked by the sharp declines in the Q_P curve (Figure 17) eventually collides and merges with an expanding structure composed of the fused barriers. This pile-up (Figure 30) is caused by the perseverance of the outermost surface of the fused barrier structure, and is attributed to limited dissociation because the low permeability does not allow sufficient amounts of warmer fluids from deeper within the formation to reach the barrier structure and fuel dissociation. Dissociation of the fused barrier structure begins to be observed only at an advanced time (Figure 30k). This is not a problem in the more permeable system of the reference Case C (Figure 20), in which warmer fluids arriving at the outer surface of the farthest stationary barrier lead to its destruction.

Additional Important Issues
Implications of the evolution pattern of R_{WGC} over time. Review of the evolution of the R_{WGC} pattern over time in Figure 29 indicates that a universal feature of the depressurization-based production from Class 3 deposits is the continuously declining water production relative to the gas produc-

tion. Thus, R_{WGC} continuously (and monotonically) declines over time until the exhaustion of the resource. This observation is valid under any of the conditions and production methods investigated in this study, and is entirely analogous to the observation from the study of production from Class 2 deposits[14]. This is opposite to the behavior of conventional gas reservoirs, in which R_{WGC} invariably increases over time. The obvious conclusion is that hydrate deposits reserve their worst performance for the initial stages of production, but then they rapidly and continuously improve over time.

Salinity X_P of the produced water. Gas production from Class 3 deposits is invariably accompanied by the concurrent production of large volumes of water originating to a considerable degree from hydrate dissociation. The salinity of the produced water may pose significant problems and considerable disposal complications. Because water from dissociation is fresh, its disposal may not face significant regulatory challenges if it is to be made at or near the ocean surface (especially if the ocean is deep at the disposal location). However, such disposal can burden gas production with the cost and environmental loading associated with lifting such large water volumes to the surface, which are substantial in cases such as the Tigershark formation we used as a reference in this study (lying in 2740 m of water at a depth of 3230 m).

Considerable cost savings and environmental benefits could be realized if the produced water could be disposed of near the ocean floor. However, this is contingent upon meeting regulatory standards concerning the health and vitality of chemosynthetic communities that are often encountered on the ocean floor near hydrate accumulations, or of any other oceanic flora and fauna in the vicinity. Such biota may not be able to survive a significant change in salinity if the released water is substantially less saline than the ocean water in their immediate surroundings. Thus, it is important to determine the salinity of the water that is produced along with the gas from hydrate deposits.

Figure 31 shows the evolution of the salinity X_P of the water (expressed as its mass fraction in the aqueous phase) in the production stream, and demonstrates the dependence of the evolution of X_P on the sensitivity parameters investigated in this study. These results indicate that, unlike the case of production from Class 2 deposits[14], the water produced at the well in the course of gas production from Class 3 deposits exhibits a rather sharp decline in salinity, easily declining by 35-40% over its original value within 3-4 years. As expected, the decline is more pronounced when S_{H0} increases because the amount of originally free native water is lower, while a larger portion of the total water inventory is associated with the hydrate (and there is no access to a saline water aquifer, as is the case in Class 2 deposits[14]). Upon dissociation, the fraction of the released fresh water to the total water flow to the well increases, driving down the salinity. Higher k leads to enhanced dissociation and release of increased quantities of fresh water, leading to the sharp long-term decline in salinity in less permeable systems observed in Figure 31.

It is unlikely that biota near the ocean floor will be unaffected by the salinity changes indicated in Figure 31. Thus, it is almost inevitable that mixing with appropriate quantities of ocean water will be necessary in order to meet regulatory

standards of release near the chemosynthetic communities at the ocean floor.

Summary and Conclusions

(1) We investigated three different methods of gas production from Class 3 deposits. The first method involved thermal stimulation by circulating warm ocean water in the well, the second involved heat addition without fluid injection (e.g., electrical heating), and the third method involved constant-P depressurization. The entire well interval was perforated. For relevance, the properties and initial conditions of the Class 3 deposit we investigated were those in the HBL of the Tigershark formation in the Gulf of Mexico.

(2) In Case A, warm ocean water was circulated at a rate of $Q_I = 6$ kg/s and a specific enthalpy of $H_W = 2.75$ J/Kg. The CH_4 production rate Q_P initially increased, reached a maximum level of 7×10^{-3} ST m^3/s (21 MSCFD), and then began to decline. Heat addition at a uniform rate of $Q_H = 600$ W/m of the wellbore resulted in an oscillating Q_P that rapidly converged to a mean of 1.6×10^{-3} ST m^3/s (5 MSCFD) of CH_4 and had a mild declining trend. In both Cases A and B, Q_P was orders of magnitude lower than the 2-6 ST m^3/s (6-18 MMSCFD) that can be attained from a Class 2 formation, and cannot satisfy minimum economic viability conditions under any circumstances.

(3) The reasons for the poor performance of pure thermal stimulation include (a) limited access to the main HBL body, (b) inefficiency, (c) slow heat transfer rates, (d) large energy needs, (e) inevitable and increasing heat losses through the boundaries, and (f) the need to raise the temperature of not only the hydrate but also of the inert phases (i.e., the porous medium and the non-hydrate phases), which constitute the dominant portion of the mass of a given formation volume. If the heat-transfer mechanism is advection (e.g., warm water injection), then the injected fluid may have adverse effects on the relative permeability of the released gas, in addition to limited thermal conductivity because of the insulating properties of gas and flow stagnation as circulating water and escaping gases move in opposite directions. Heat transfer is significantly slower and less efficient if it is based on conduction, e.g., through electrical heating.

(4) Review of the S_H distribution and flow patterns for Cases A and B indicates limited hydrate dissociation over a long period, while fresh water release reduces the water salinity ahead of the dissociation front. The released gas moves along a band that hugs the dissociation front, and accumulates near the top of the HBL. Review of the T distribution confirms the limited thermal penetration of the HBL, and provides an explanation for the low Q_P.

(5) In Case C, gas was produced from the Class 3 accumulation by means of constant-P depressurization. The CH_4 production rate Q_P follows a cyclical pattern that includes a long rising segment, followed by a short precipitous drop. Q_P reaches a maximum level of $Q_P = 5$ ST m^3/s of CH_4 (15 MMSCFD). During the 6,000-day production period, the hydrate was exhausted, and a total of $V_P = 1.37 \times 10^9$ ST m^3 (4.84×10^{10} ST ft^3) of CH_4 were produced at an average rate $Q_{avg} = 2.61$ ST m^3/s (8.10 MMSCFD).

(6) For Case C, the water mass production rate Q_W shows an exponential-like decline with time from a large initial level of $Q_W = 23$ kg/s (12,200 BPD) to an average of about $Q_W = 2.5$ kg/s (1,300 BPD) after $t = 1,000$ days. Even at its highest, this Q_W level is manageable, and so is the cumulative mass of produced water M_W. Production from Class 3 hydrates by constant-P depressurization is at its most challenging upon initiation, and the picture continuously improves with time.

(7) In contrast to production from Class 2 deposits with the same initial conditions, which is characterized by long lead times of low production Q_P, constant-P production from Class 3 deposits begins in earnest from the moment depressurization is applied.

(8) These production results clearly indicate that there is nothing intrinsically prohibitive in the production from Class 3 hydrates, and provide convincing evidence that the earlier impressions of low production potential of such hydrate deposits were the result of inappropriate production methods. Thus, gas can be produced from Class 3 hydrates using conventional well technology.

(9) In Case C, the precipitous Q_P drops occur when a traveling dual barrier (composed of concentric cylindrical structures formed from secondary hydrates) evolve and restrict flow to the well. This dual barrier is a unique feature of constant-P production from Class 3 hydrate accumulations.

(10) As in Class 2 deposits, dissociation in Case C is characterized by (a) the evolution of an upper dissociation interface at the top of the hydrate layer (caused by heat flows from the upper boundary) in addition to the lower dissociation interface at the bottom of the HBL, and (b) gas accumulation below the base of the overburden because of continuing dissociation and buoyancy-driven gas rise to the top of the formation. The gas accumulation pattern has particularly important (and potentially severe) implications for gas production from oceanic deposits because lack of a confining overburden could lead to gas loss through percolation though the overburden and release at the ocean floor.

(11) As in Class 2 deposits, processes and phenomena that occur within a narrow zone around the well control gas production from the entire hydrate deposit in Case C. This critical zone has a radius $r_c < 15$-20 m, and fine discretization must be used in its simulations if these near-well phenomena are to be captured and accurately described. Dissociation and flow patterns are uniform and smooth along the entire area of the horizontal interfaces for $r > r_c$.

(12) Gas production increases (and the corresponding water-to-gas ratio R_{WGC} decreases) with an increasing (a) hydrate temperature (which defines its stability for a given pressure), and (c) intrinsic permeability. Lower initial hydrate saturations lead initially to higher gas production and a lower R_{WGC}, but the effect is later reversed as the hydrate is depleted.

(13) Water released at the well in the course of gas production from hydrate dissociation exhibits a substantial re-

ductions reduction in salinity, which can exceed 40% after 3-4 years. This is unlikely to allow water releases near the ocean floor without the risk of adversely affecting chemosynthetic communities and other biota, and an appropriate mixing regime with native saline water will need to be developed to mitigate the problem.

Nomenclature

Δr = Radial increment (m)
Δz = Vertical discretization, i.e., in the z-direction (m)
A_D = area of the dissociation zone (m^2)
C = specific heat (J/kg/K)
F_A = area factor (dimensionless)
h = thickness of the hydrate bearing layer (m)
H_L = heat flux at the well
H_W = specific enthalpy of water circulating in the well (J/kg)
k = intrinsic permeability (m^2)
k_{eff} = effective permeability, accounting for the presence of ice and/or hydrate (m^2)
k_r = relative permeability (m^2)
k_Θ = thermal conductivity (W/m/K)
$k_{\Theta RD}$ = thermal conductivity of dry porous medium (W/m/K)
$k_{\Theta RW}$ = thermal conductivity of fully saturated porous medium (W/m/K)
M_W = cumulative mass of water released into the ocean through the annular gravel pack (kg)
N_H = hydration number
P = pressure (Pa)
P_0 = initial pressure in hydrate-bearing sediments (Pa)
P_Q = pressure at the quadruple point (Pa)
Q_Θ = rate of heat injection into the formation next to the well (W/m of wellbore)
Q_I = mass rate of injected warm water at the well (kg/s)
Q_M = mass rate of fluid withdrawal at the well (kg/s)
Q_P = volumetric rate of CH$_4$ production at the well (ST m^3/s)
Q_R = volumetric rate of CH$_4$ release from hydrate dissociation into the reservoir (ST m^3/s)
Q_W = mass rate of water release into the ocean through the annular gravel pack (kg/s)
Q_V = rate of CH$_4$ release from hydrate dissociation (ST m^3/s)
r,z = coordinates (m)
r_c = critical radius of maximum activity around the wellbore (m)
r_D = radius of the dissociation around the well (m)
r_w = radius of the well assembly (m)
r_{max} = maximum radius of the simulation domain (m)
R_{WGC} = ratio of water removed per volume of gas produced
S = phase saturation
t = time (s)
T = temperature (K or ^{o}C)
V_R = cumulative volume of CH$_4$ released from hydrate dissociation (ST m^3)
V_P = cumulative volume of CH$_4$ released into the ocean through the annular gravel pack (ST m^3)
X_i = water salinity (mass fraction)

Greek Symbols

λ = van Genuchten exponent – Table 1
ϕ = porosity

Subscripts and Superscripts

0 = denotes initial state
A = aqueous phase
B = HBL base
D = dissociation
$D12$ = dissociation in Classes 1 and 2
e = equilibrium conditions
cap = capillary
G = gas phase
H = solid hydrate phase
irG = irreducible gas
irA = irreducible aqueous phase
n = permeability reduction exponent – Table 1
ref = reference Case C
R = rock

References

1. Sloan, E.D., *Clathrate Hydrates of Nautral Gases.* Marcel Decker, Inc., New York, NY (1998).
2. Milkov, A. V., "Global estimates of hydrate-bound gas in marine sediments: How much is really out there," *Earth Science Reviews* **66**(3), 183 (2004).
3. Klauda, J.B., Sandler, S.I., "Global distribution of methane hydrate in ocean sediment," *Energy & Fuels* **19**, 469 (2005).
4. Makogon, Y.F., "Gas hydrates: frozen energy," *Recherche* **18**(192), 1192 (1987).
5. Dallimore, S.R., Collett, T.S., Eds., "Scientific Results from the Mallik 2002 Gas Hydrate Production Research Well Program, Mackenzie Delta, Northwest Territories, Canada," *Geological Survey of Canada Bulletin* **585** (2005).
6. Moridis, G.J., and Collett, T.S.: "Strategies for gas production from hydrate accumulations under various geologic conditions", Report LBNL-52568, Lawrence Berkeley National Laboratory, Berkeley, CA (2003).
7. Moridis, G.J., Kowalsky, M.B., Pruess, K., "Depressurization-induced gas production from Class 1 hydrate deposits," (LBNL-59780) SPE 97266, 2005 SPE Annual Technical Conference and Exhibition, Dallas, Texas, U.S.A., October 9-12, 2005.
8. Moridis, G.J., Sloan, E.D., "Gas production potential of disperse low-saturation hydrate accumulations in oceanic sediments," (LBNL-52586) in press, *J. Energy Conversion & Management* (2007).
9. Moridis, G.J., T. Collett, S. Dallimore, T. Satoh, S. Hancock and B. Weatherhill, "Numerical studies of gas production from sev-

eral methane hydrate zones at the Mallik Site, Mackenzie Delta, Canada," (LBNL-50257) *J. Petroleum Sci Eng.* **43**, 219 (2004).

10. Moridis, G.J., "Numerical studies of gas production from Class 2 and Class 3 hydrate accumulations at the Mallik Site, Mackenzie Delta, Canada," *SPEREE*, **7**(13), 175 (2004).

11. Moridis, G.J., Seol, Y., Kneafsey, T., "Studies of reaction kinetics of methane hydrate dissociation in porous media", Report LBNL-57298, Lawrence Berkeley National Laboratory, Berkeley, CA (2005).

12. Moridis, G.J., Kowalsky, M.B., Pruess, K., "TOUGH-Fx/HYDRATE v1.0 User's Manual: A code for the simulation of system behavior in hydrate-bearing geologic media," Report LBNL-3185, Lawrence Berkeley National Laboratory, Berkeley, CA (2005).

13. Makogon, Y.F., *Hydrates of Hydrocarbons*. Penn Well Publishing Co. Tulsa, OK. (1997).

14. Moridis, G.J., Reagan, M.T., "Gas Production From Oceanic Class 2 Hydrate Accumulations," OTC 18866, 2007 Offshore Technology Conference, Houston, Texas, U.S.A., 30 April–3 May 2007.

15. Moridis, G.J., T.S. Collett, S.R. Dallimore, T. Inoue and T. Mroz, "Analysis and Interpretation of the Thermal Test of Gas Hydrate Dissociation in the JAPEX/JNOC/GSC et al. Mallik 5L-38 Gas Hydrate Production Research Well", in Scientific Results from the Mallik 2002 Gas Hydrate Production Research Well Program, Mackenzie Delta, Northwest Territories, Canada. *Geological Survey of Canada, Bulletin* **585**, S.R. Dallimore and T. Collett, Editors, 2005 (LBNL-57296).

16. Booth J.S., Rowe M.M., Fischer K.M., "Offshore gas hydrate sample database". USGS Open-File Report 96-272, June 1996.

17. Smith, S., Boswell, R., Collett, T., Lee, M., Jones, E., "Alaminos Canyon Block 818: A Documented Example of Gas Hydrate Saturated Sand in the Gulf of Mexico," *Fire In The Ice*: NETL Methane Hydrates R&D Program Newsletter, 12 (Fall 2006).

18. Collett, T.S., Lee, M.W., *Well Log Analysis: Tiger Shark AC 818 No. 1*, U.S. Geological Survey, internal memo (2006).

19. Moridis, G.J., Kowalsky, M.B., "Response of Oceanic Hydrate-Bearing Sediments to Thermal Stresses," (LBNL-60150) OTC 18193, 2006 Offshore Technology Conference, Houston, Texas, U.S.A., May 1-4, 2006.

20. Kim, H.C., Bishnoi, P.R., Heidemann, R.A., and Rizvi, S.S.H.: "Kinetics of Methane Hydrate Decomposition", *Chem. Eng. Sci.*, **42**(7), 1645 (1987).

21. Clarke, M.A., and Bishnoi, P.R.: "Determination of the Intrinsic Rate of Methane Gas Hydrate Decomposition", *Chem. Eng. Sci.*, **55**, 4869 (2000).

22. Kowalsky, M.B., Moridis, G.J., "Comparison of Kinetic and Equilibrium Reaction Models in Simulating the Behavior of Gas Hydrates in Porous Media, " (LBNL-60361) in press, *J. Energy Conversion & Management* (2006).

23. van Genuchten, M.Th.: "A Closed-Form Equation for Predicting the Hydraulic Conductivity of Unsaturated Soils", *Soil Sci. Soc.*, **44**, 892 (1980).

Table 1 – Hydrate Deposit Properties

Parameter	Value
Hydrate zone thickness	18.25 m
Initial pressure P_B (at base of HBL)	3.3×10^7 Pa
Initial temperature T_B (at base of HBL)	294.15 K (21 $^\circ$C)
Gas composition	100% CH_4
Water salinity (mass fraction)	0.03
Initial saturations in the HBL	$S_H = 0.7$, $S_A = 0.3$
Intrinsic permeability $k_r = k_z$ (HBL)	7.5×10^{-13} m^2 (= 0.75 D)
Intrinsic permeability $k_r = k_z$ (overburden & underburden)	0 m^2 (= 0 D)
Grain density ρ_R (all formations)	2750 kg/m^3
Dry thermal conductivity $k_{\Theta RD}$ (all formations)	0.5 W/m/K
Wet thermal conductivity $k_{\Theta RW}$ (all formations)	3.1 W/m/K
Composite thermal conductivity model [13]	$k_{\Theta C} = k_{\Theta RD} + (S_A^{1/2} + S_H^{1/2})$ $(k_{\Theta RW} - k_{\Theta RD}) + \phi\, S_I\, k_{\Theta I}$
Capillary pressure model [12,23]	$P_{cap} = -P_0 \left[(S^*)^{-1/\lambda} - 1 \right]^{-\lambda}$ $S^* = \dfrac{(S_A - S_{irA})}{(S_{mxA} - S_{irA})}$
S_{irA}	1
λ	0.45
P_0	10^5 Pa
Relative permeability Model [12]	$k_{rA} = (S_A^*)^n$ $k_{rG} = (S_G^*)^n$ $S_A^* = (S_A - S_{irA})/(1 - S_{irA})$ $S_G^* = (S_G - S_{irG})/(1 - S_{irA})$ OPM model
n (from Moridis et al. [15])	3.572
S_{irG}	0.02
S_{irA}	0.25
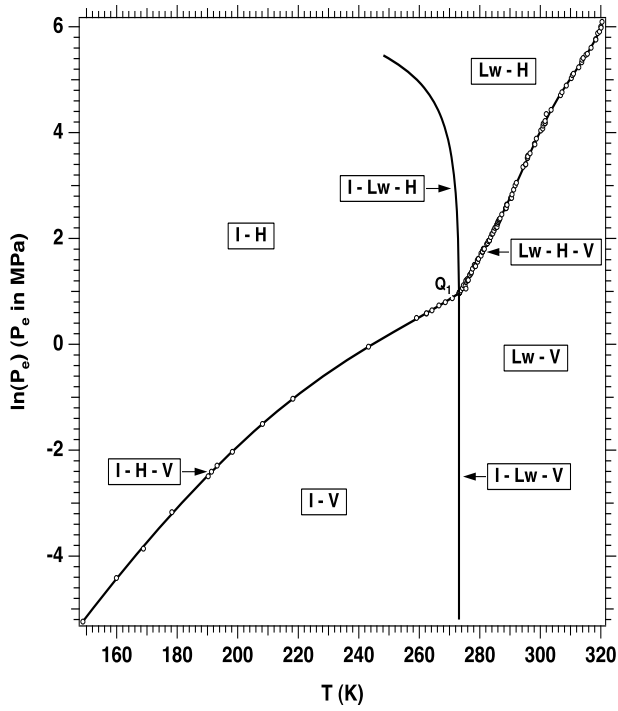
Figure 1 – Pressure-temperature equilibrium relationship in the phase diagram of the water–CH₄–hydrate system[12] (Lw: Liquid water; H: Hydrate; V: Vapor (gas phase); I: Ice; Q₁: Quadruple point = I + Lw + H + V)
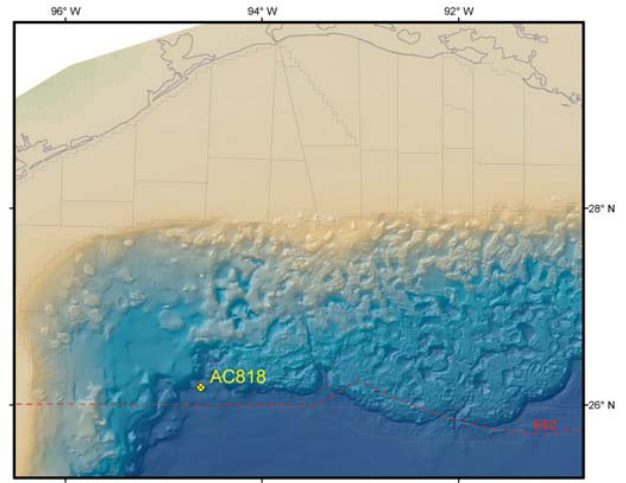
Figure 3 – Approximate location of the Tigershark exploratory well in the Alaminos Canyon block 818 in the Gulf of Mexico[15].
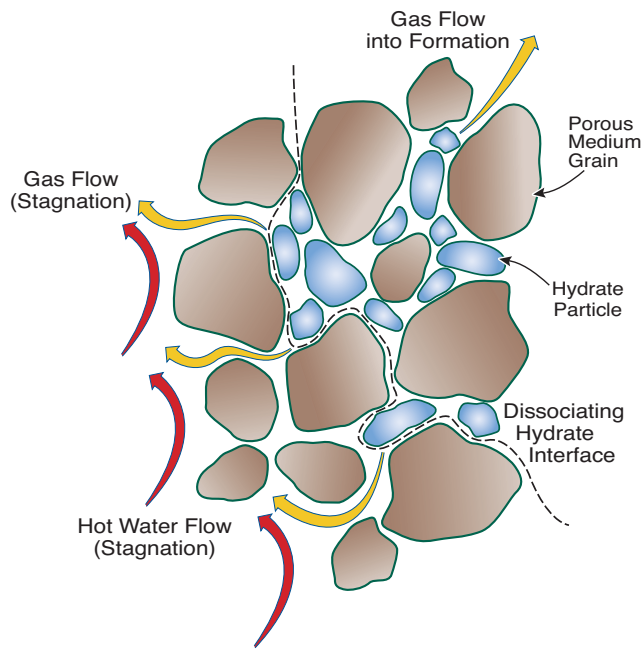

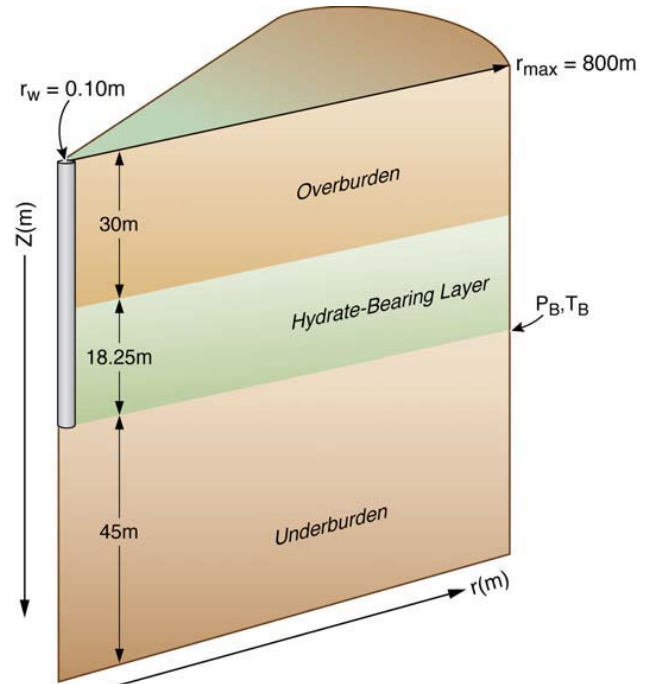**Figure 2 – A schematic of flow stagnation and gas escape into the HBL at the dissociation front[15].**

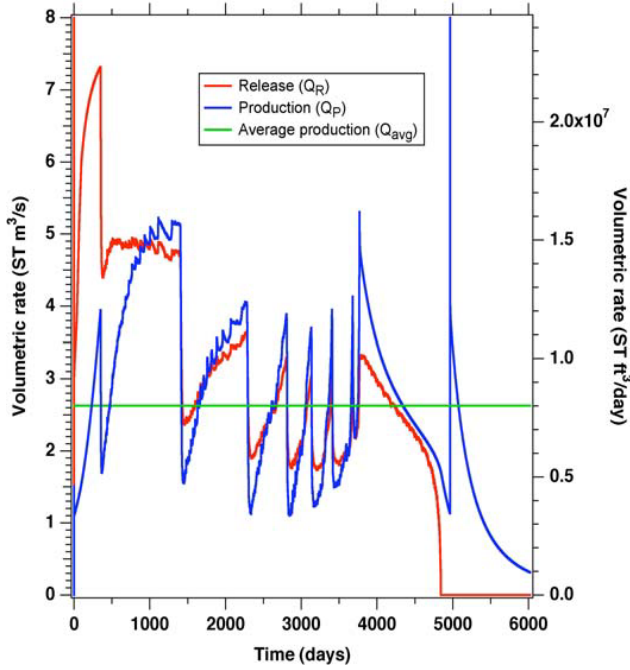**Figure 4 – A schematic of the Class 3 hydrate deposit simulated in this study.**
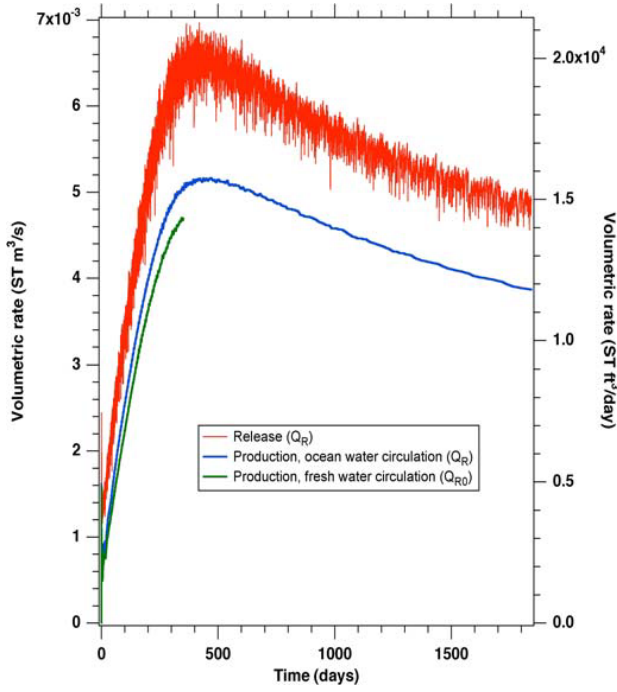
Figure 5 – Rates of (a) hydrate-originating CH₄ release in the reservoir (*Q_R*) and (b) CH₄ production at the well (*Q_P*) during production from the Class 3 oceanic hydrate deposit in Case A.
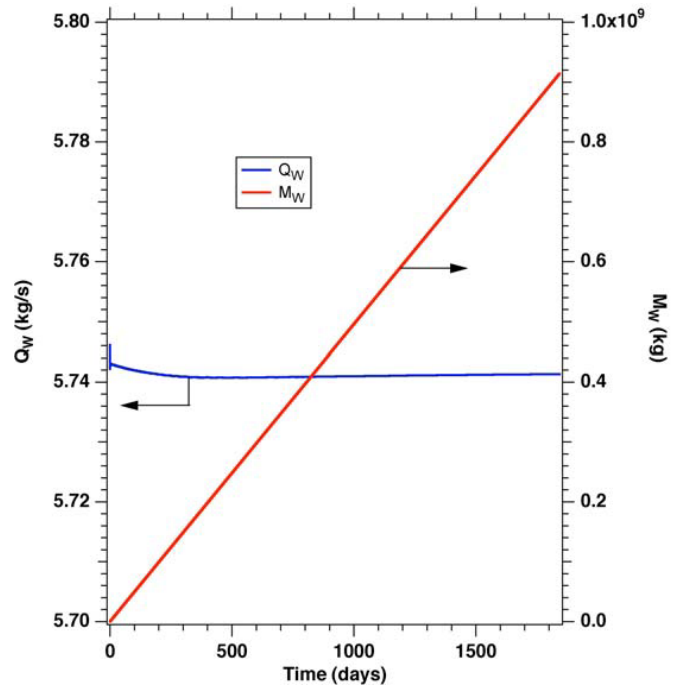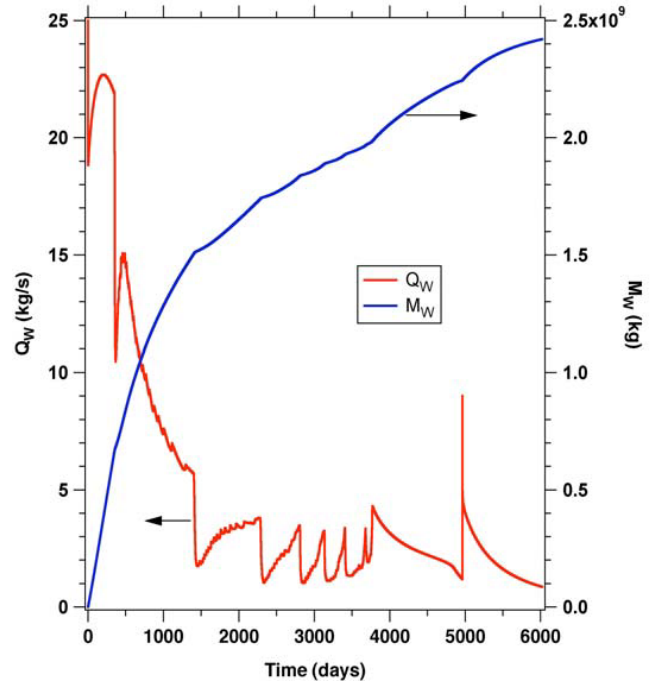
Figure 6 – (a) Rate of H₂O production (*Q_W*) and (b) cumulative mass of produced H₂O (*M_W*) during production from the Class 3 oceanic hydrate deposit in Case A.
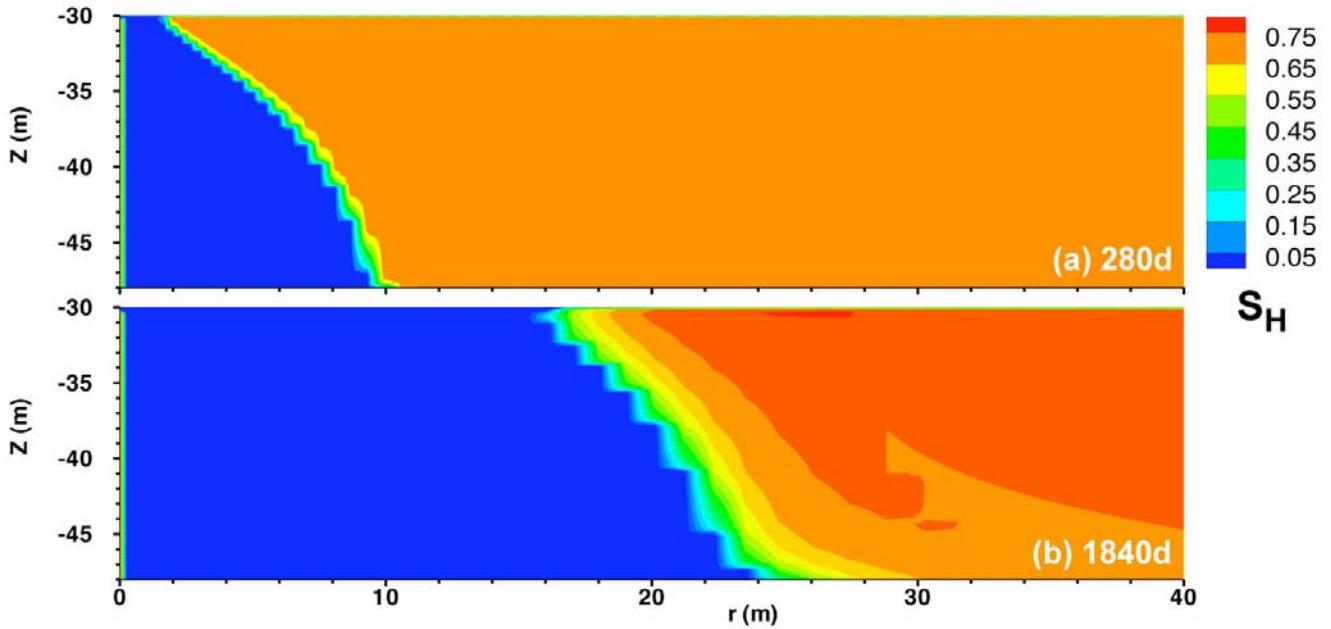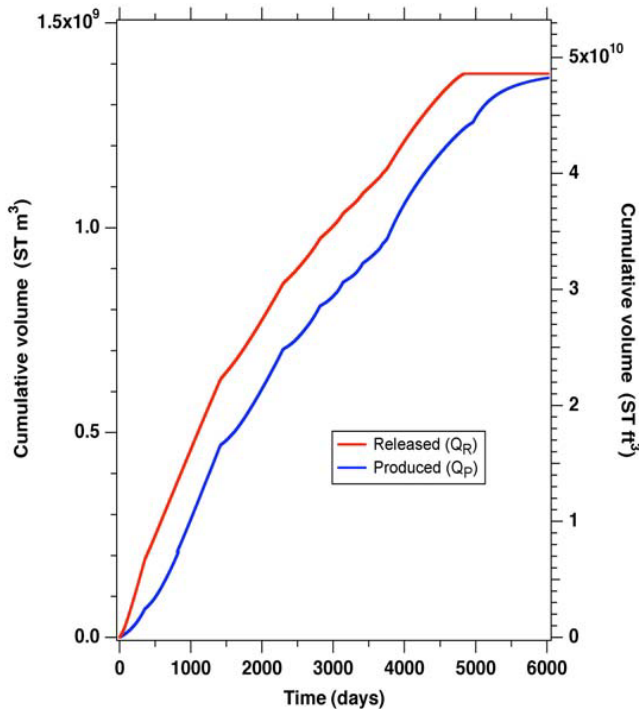

Figure 7 –Evolution of spatial distribution of S_H during gas production from the Class 3 oceanic hydrate deposit in Case A.
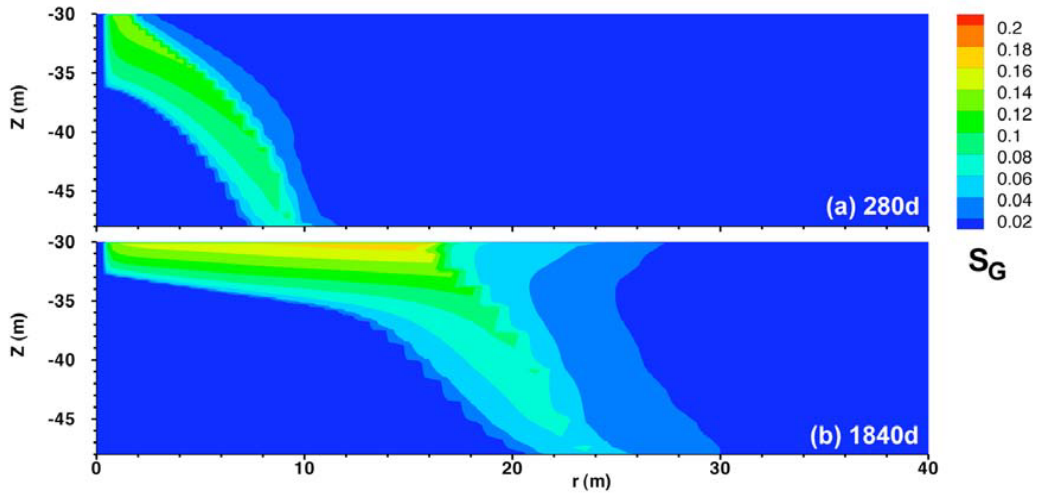
Figure 8 –Evolution of spatial distribution of S_G during gas production from the Class 3 oceanic hydrate deposit in Case A.
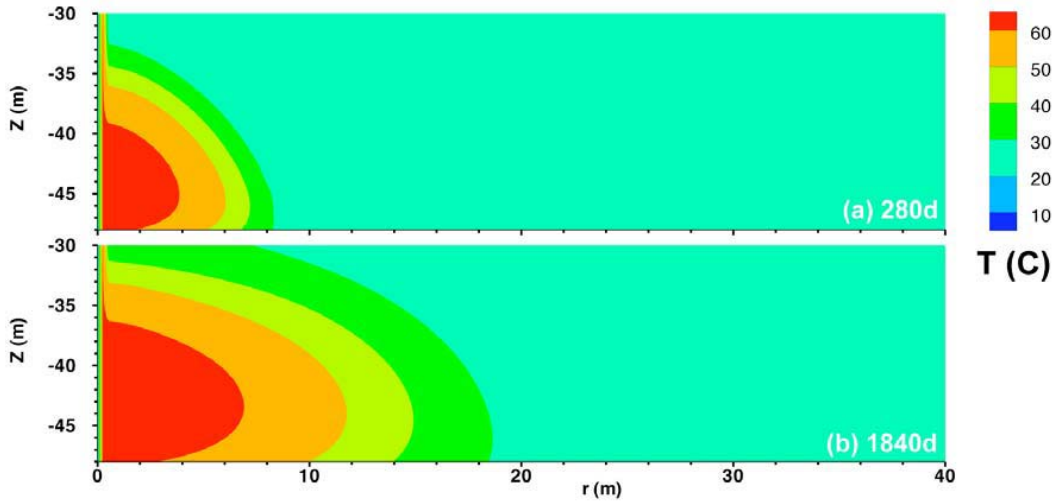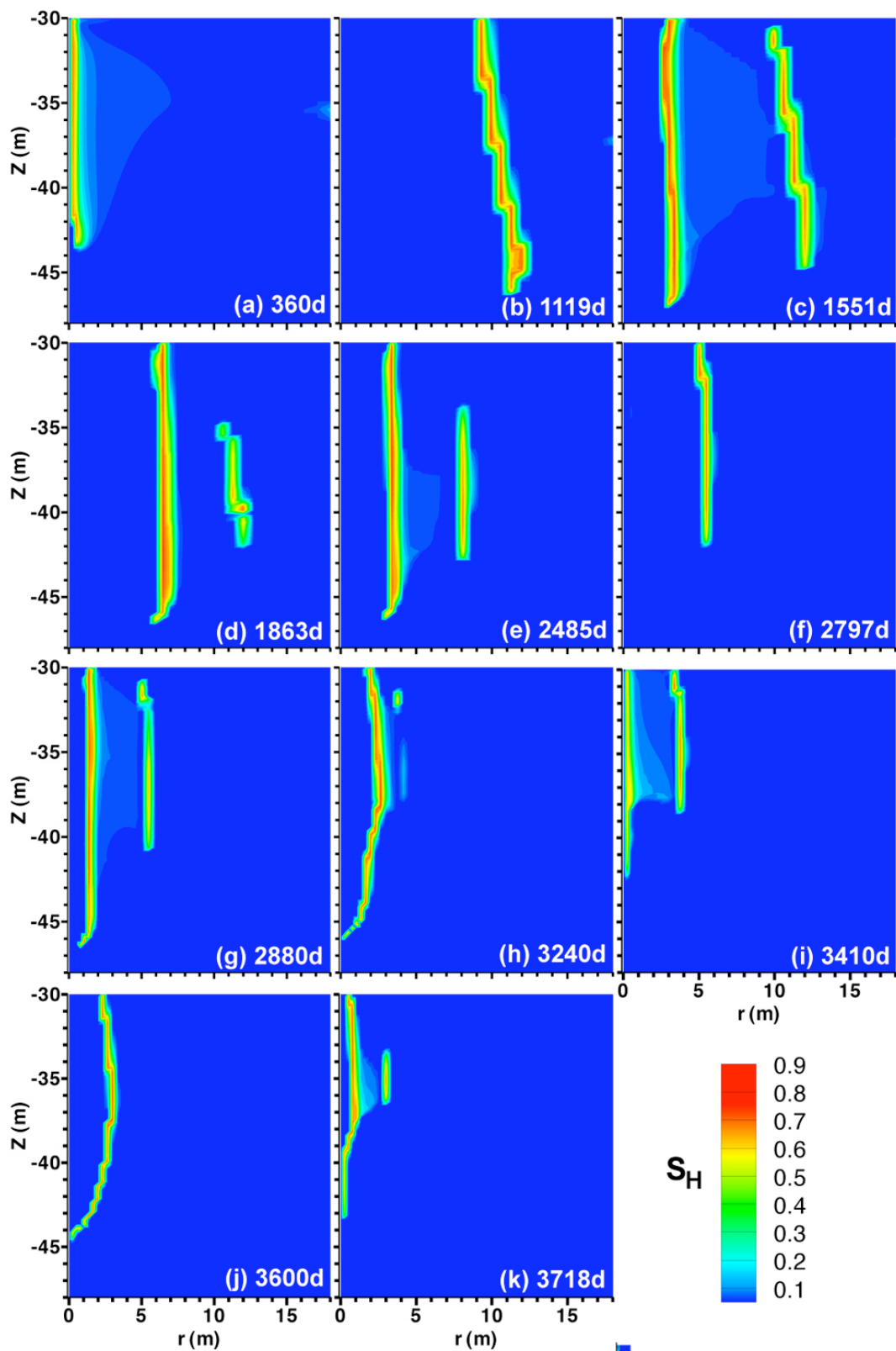

Figure 9 –Evolution of spatial distribution of T during gas production from the Class 3 oceanic hydrate deposit in Case A.
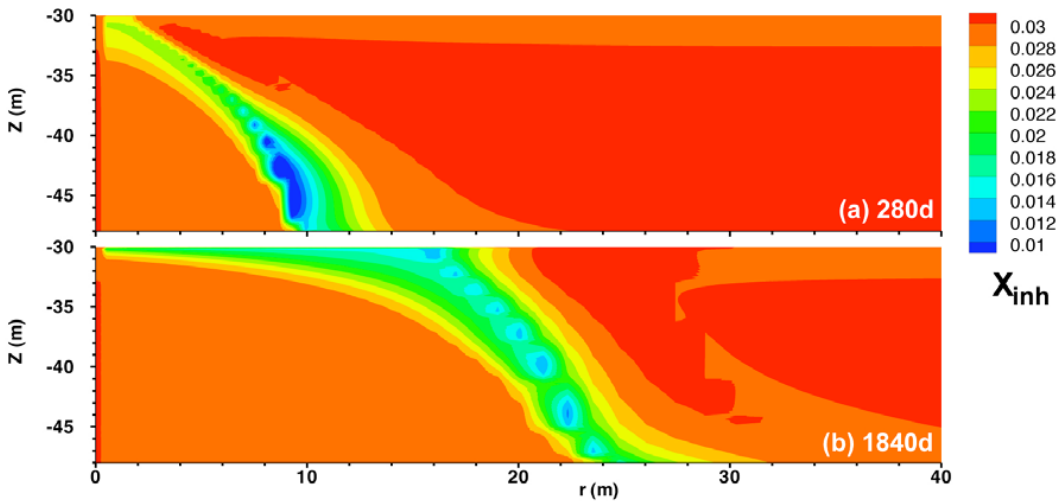
Figure 10 –Evolution of spatial distribution of X_i during gas production from the Class 3 oceanic hydrate deposit in Case A.
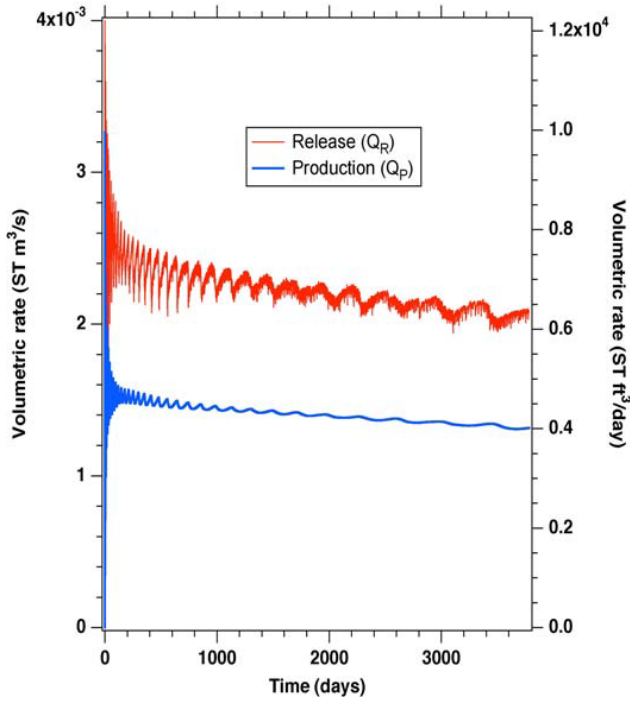
Figure 11 – Rates of (a) hydrate-originating CH$_4$ release in the reservoir (Q_R) and (b) CH$_4$ production at the well (Q_P) during production from the Class 3 oceanic hydrate deposit in Case B.
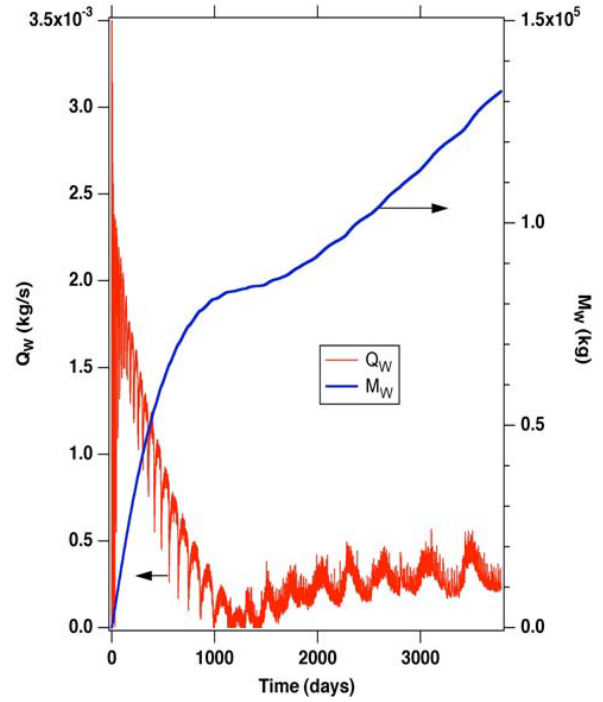
Figure 12 – (a) Rate of H$_2$O production (Q_W) and (b) cumulative mass of produced H$_2$O (M_W) during production from the Class 3 oceanic hydrate deposit in Case B.
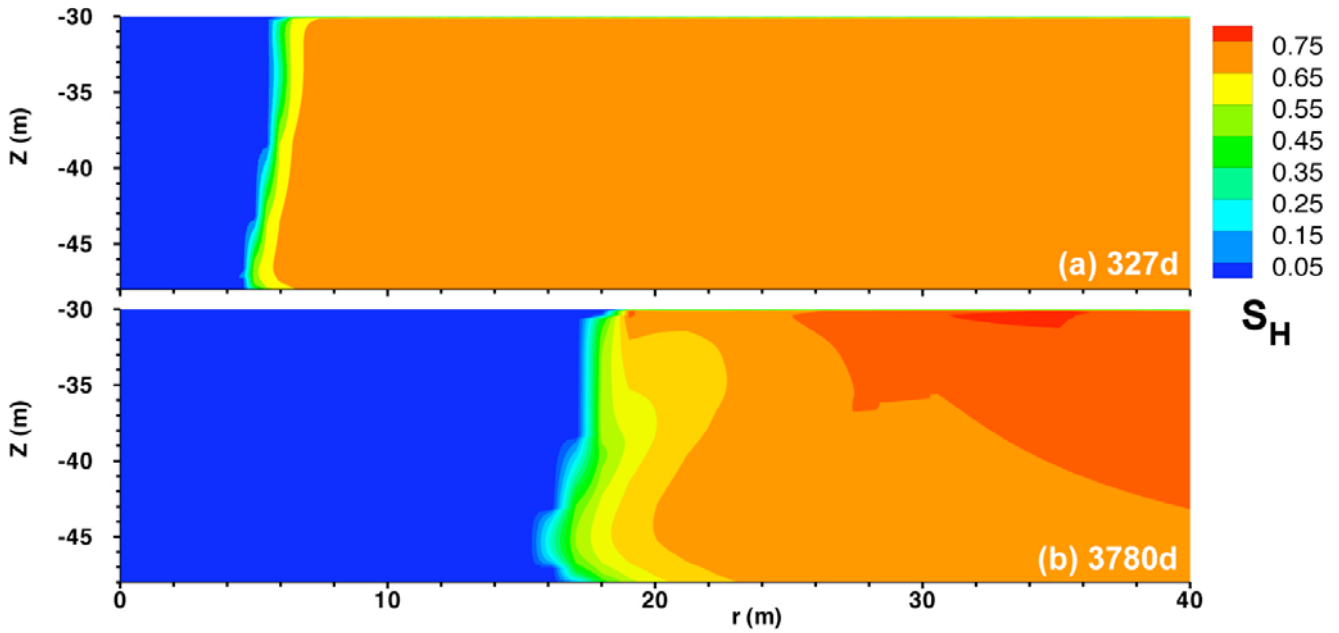
Figure 13 –Evolution of spatial distribution of S$_H$ during gas production from the Class 3 oceanic hydrate deposit in Case B.
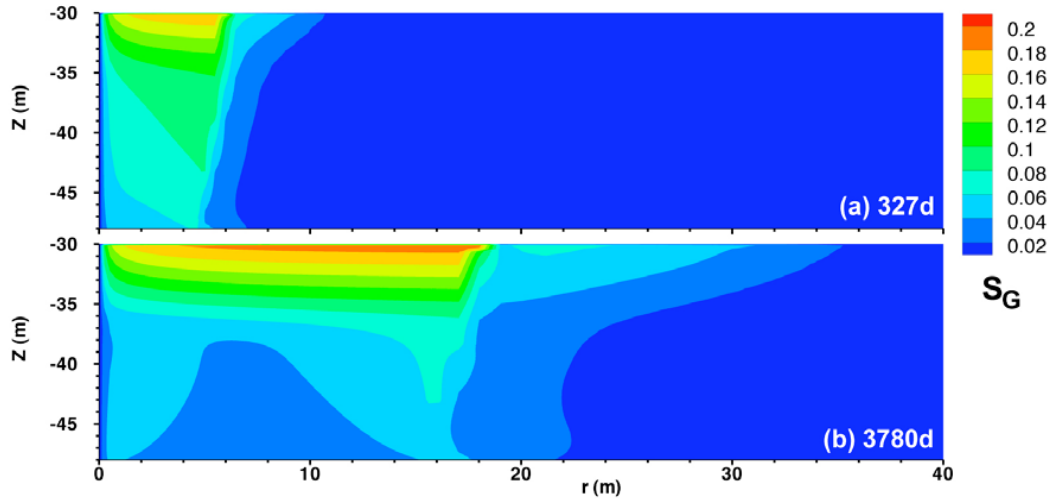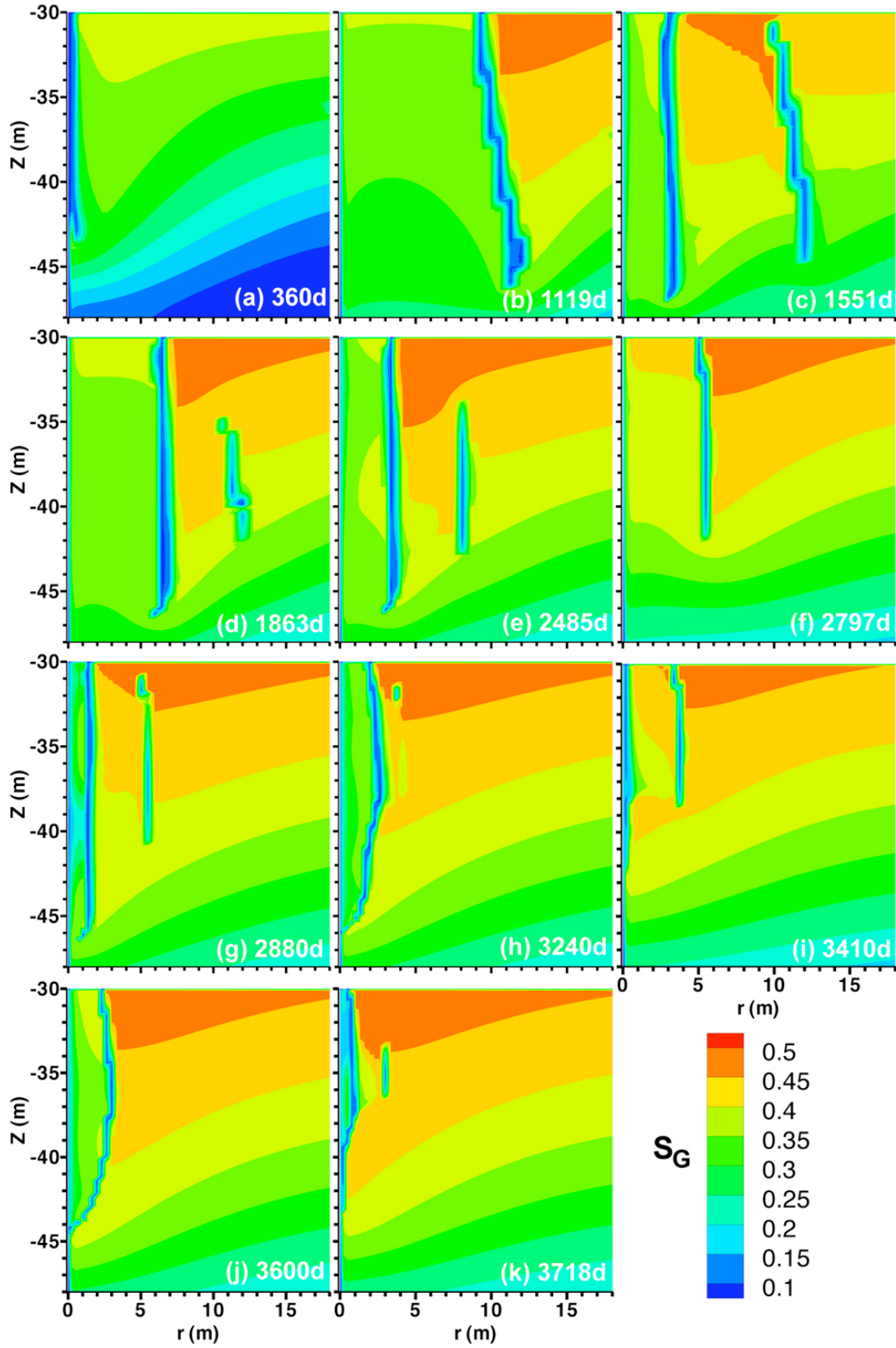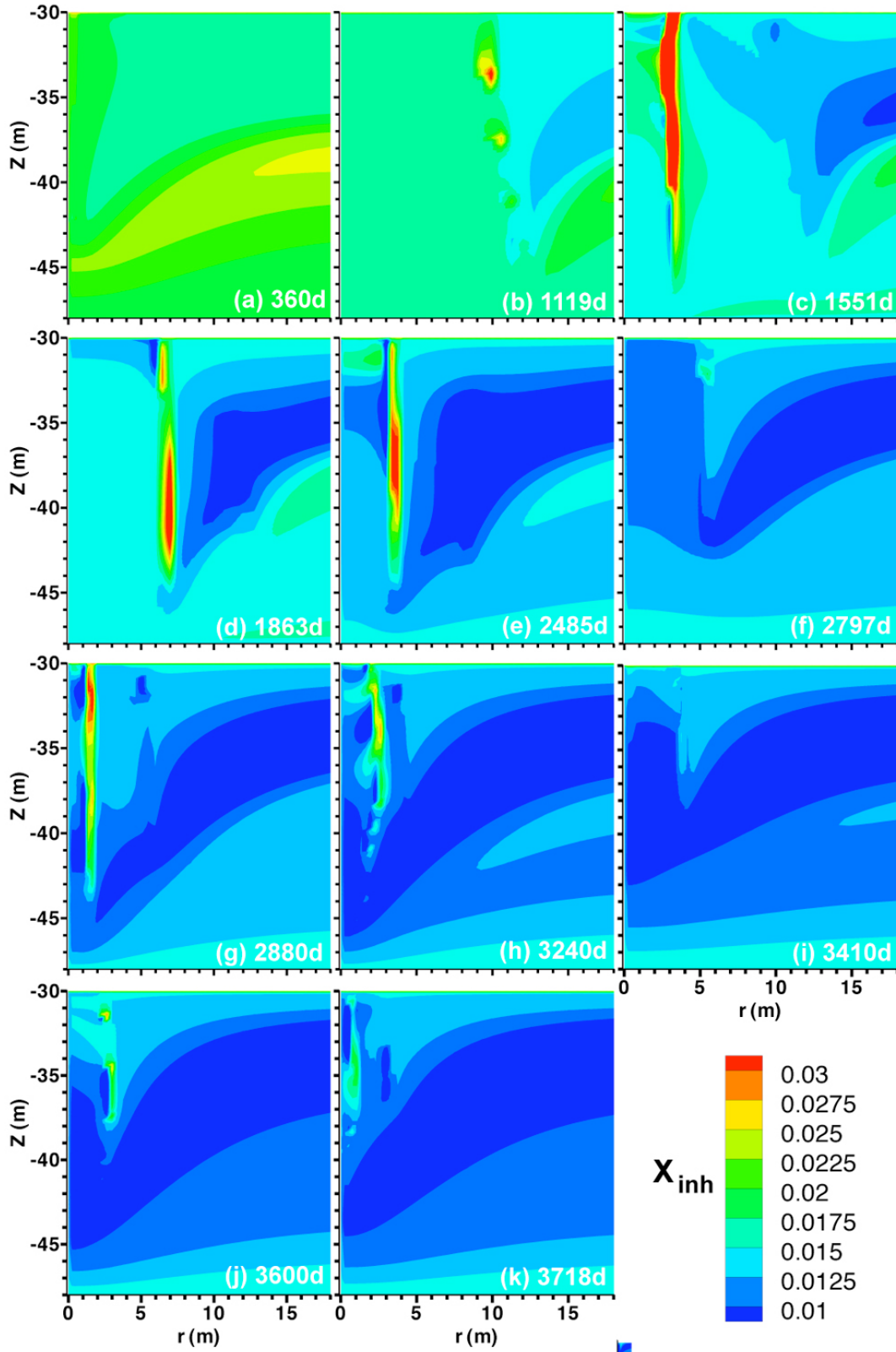
Figure 14 –Evolution of spatial distribution of S_G during gas production from the Class 3 oceanic hydrate deposit in Case B.
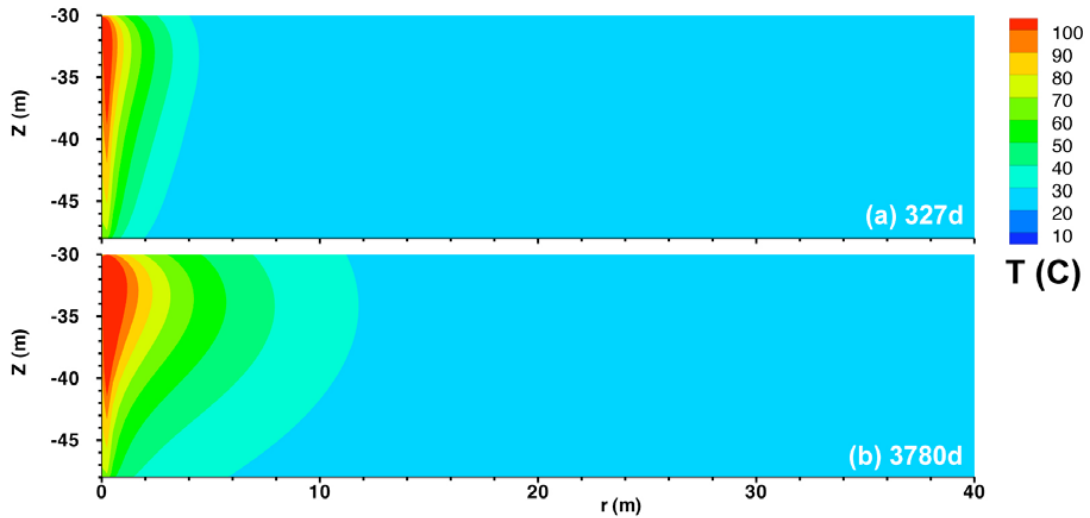
Figure 15 –Evolution of spatial distribution of T during gas production from the Class 3 oceanic hydrate deposit in Case B.
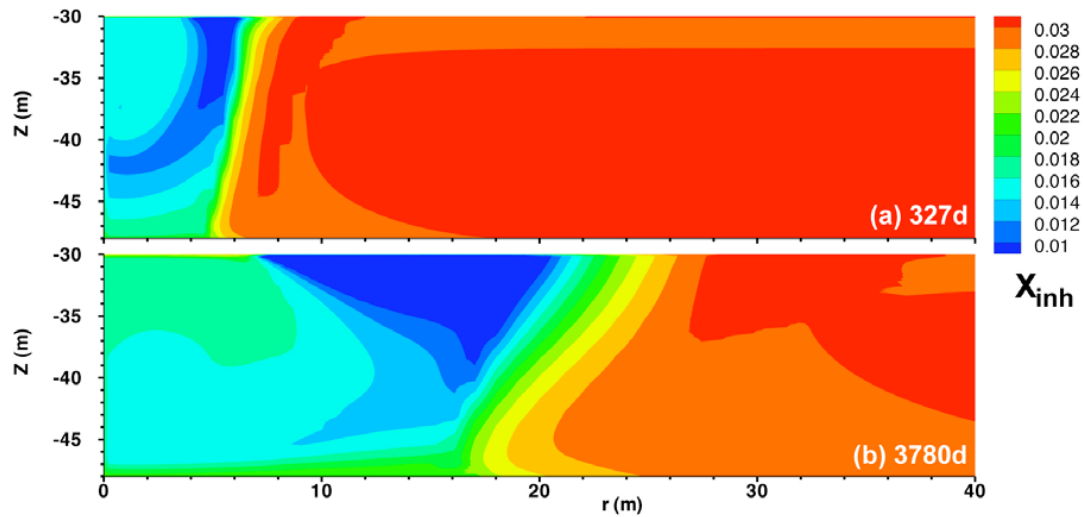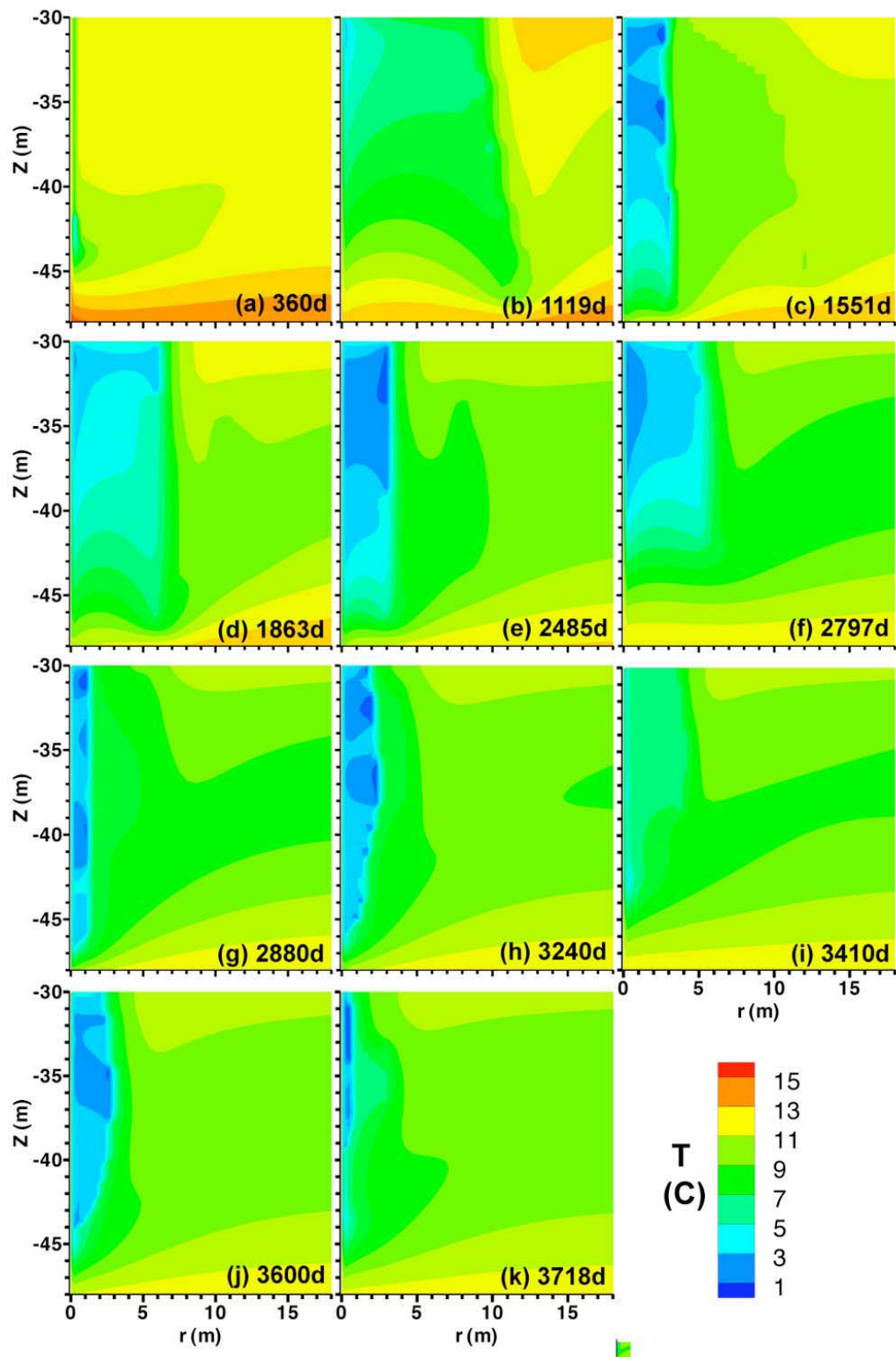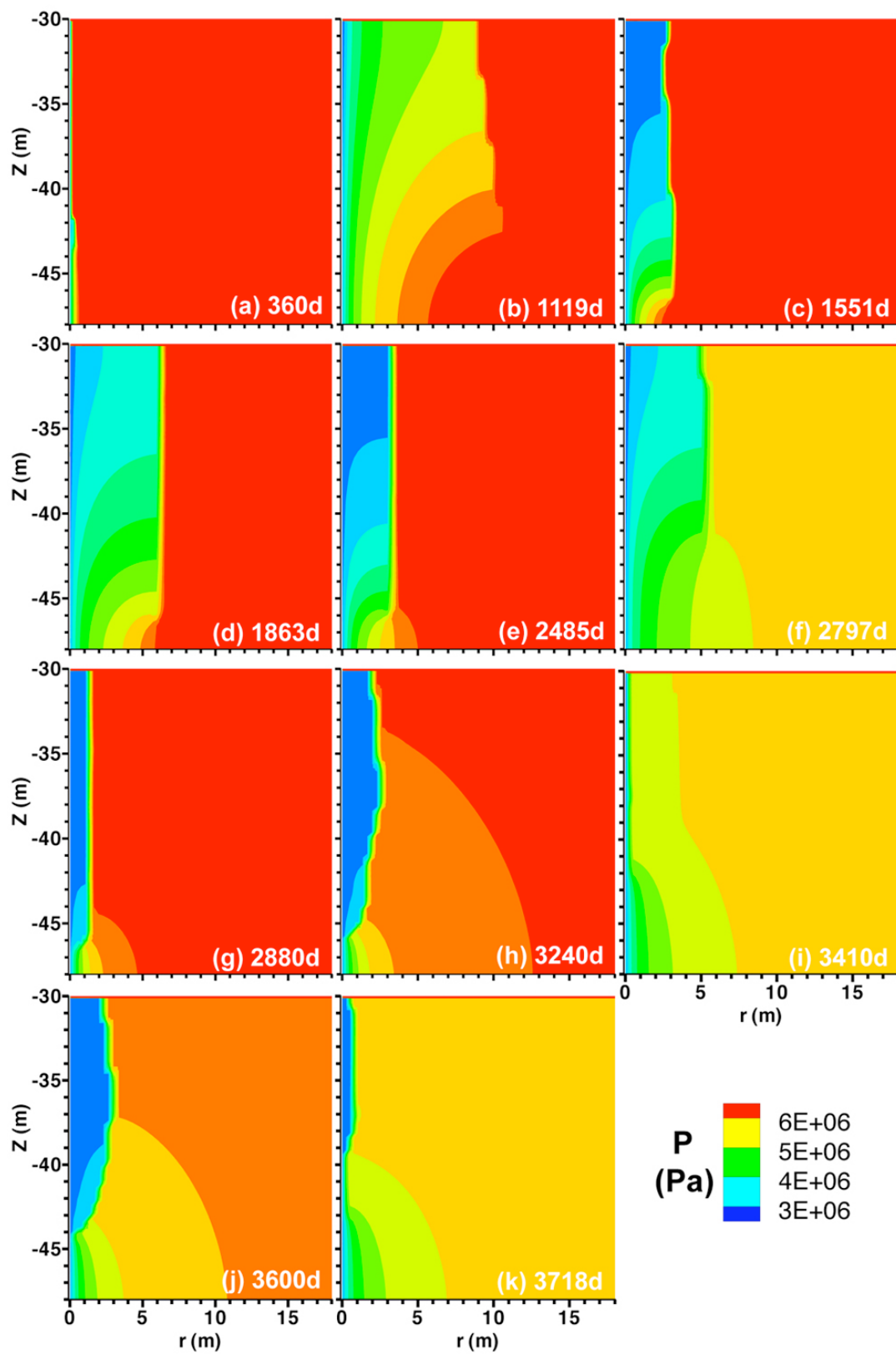

Figure 16 –Evolution of spatial distribution of X_i during gas production from the Class 3 oceanic hydrate deposit in Case B.

Figure 17 – Rates of (a) hydrate-originating CH₄ release in the reservoir (Q_R) and (b) CH₄ production at the well (Q_P) during production from the Class 3 oceanic hydrate deposit in Case C. The average production rate (Q_{avg}) over the simulation period (6000 days) is also shown.

Figure 19 – (a) Rate of H₂O production (Q_W) and (b) cumulative mass of produced H₂O (M_W) during production from the Class 3 oceanic hydrate deposit in Case C.

Figure 18 – Cumulative volumes of (a) hydrate-originating CH₄ released in the reservoir (V_R) and (b) produced CH₄ at the well (V_P) during production from the Class 3 oceanic hydrate deposit in Case C.

Figure 20 –Evolution of spatial distribution of S$_H$ during gas production from the Class 3 oceanic hydrate deposit in Case C.
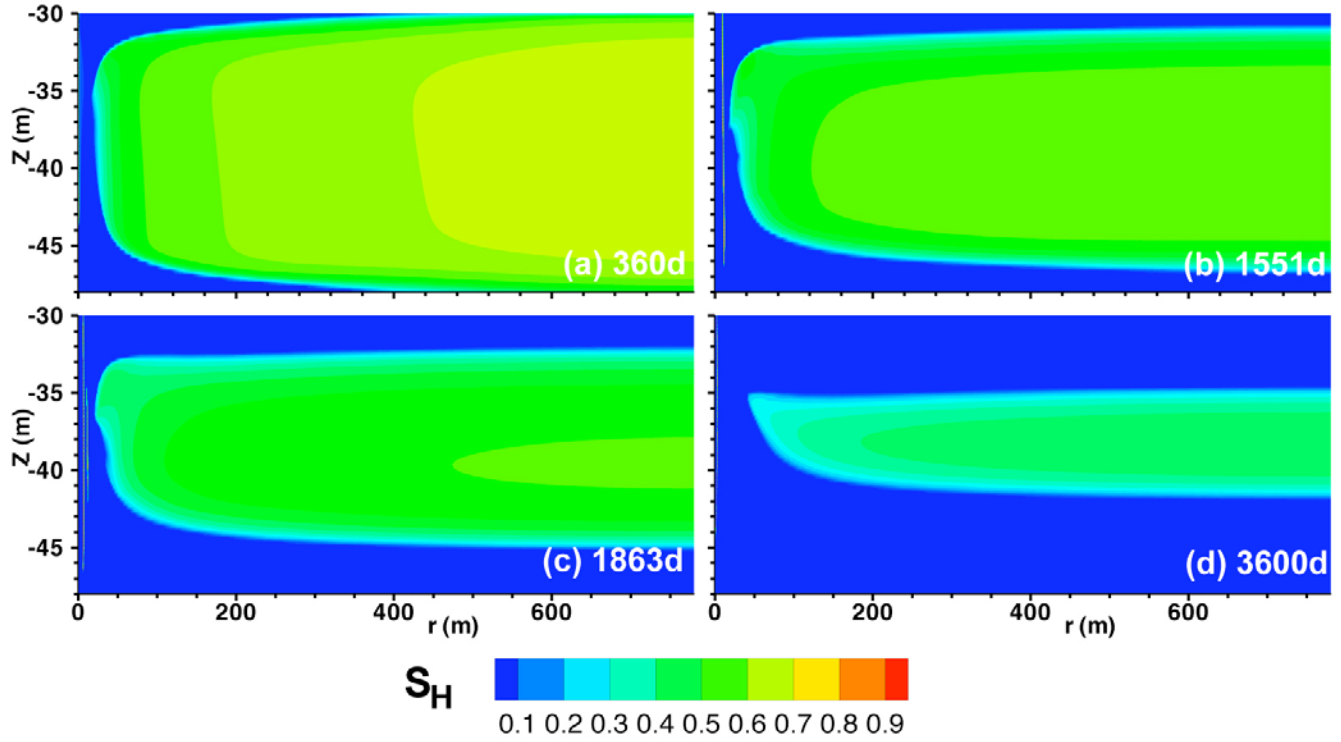
Figure 21 –Evolution of spatial distribution of S$_G$ during gas production from the Class 3 oceanic hydrate deposit in Case C.

Figure 22 –Evolution of spatial distribution of X_i during gas production from the Class 3 oceanic hydrate deposit in Case C.

Figure 23 –Evolution of spatial distribution of T during gas production from the Class 3 oceanic hydrate deposit in Case C.

Figure 24 –Evolution of spatial distribution of P during gas production from the Class 3 oceanic hydrate deposit in Case C.

Figure 25 – Evolution of the S_H distribution over the entire Class 3 hydrate deposit in Case C to demonstrate the uniformity of dissociation away from the critical near-well zone.
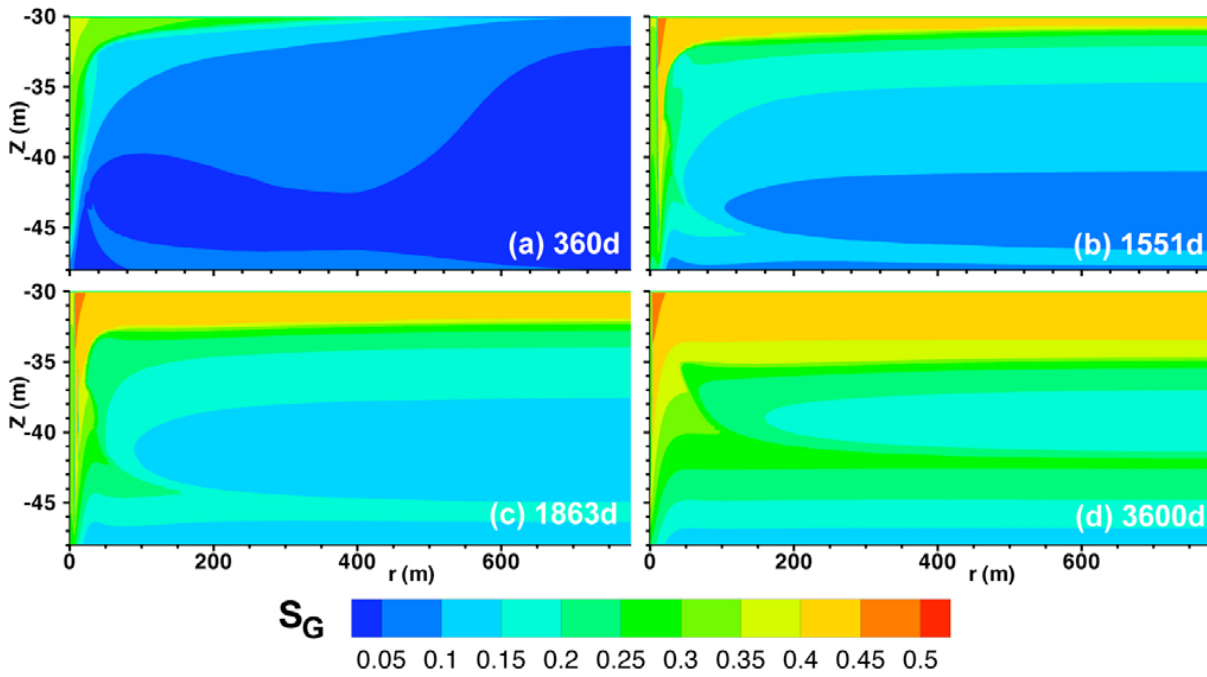
Figure 26 – Evolution of the S_G distribution over the entire Class 3 hydrate deposit in Case C to demonstrate the uniformity of gas evolution pattern and/or the smoothness of its variation away from the critical near-well zone.
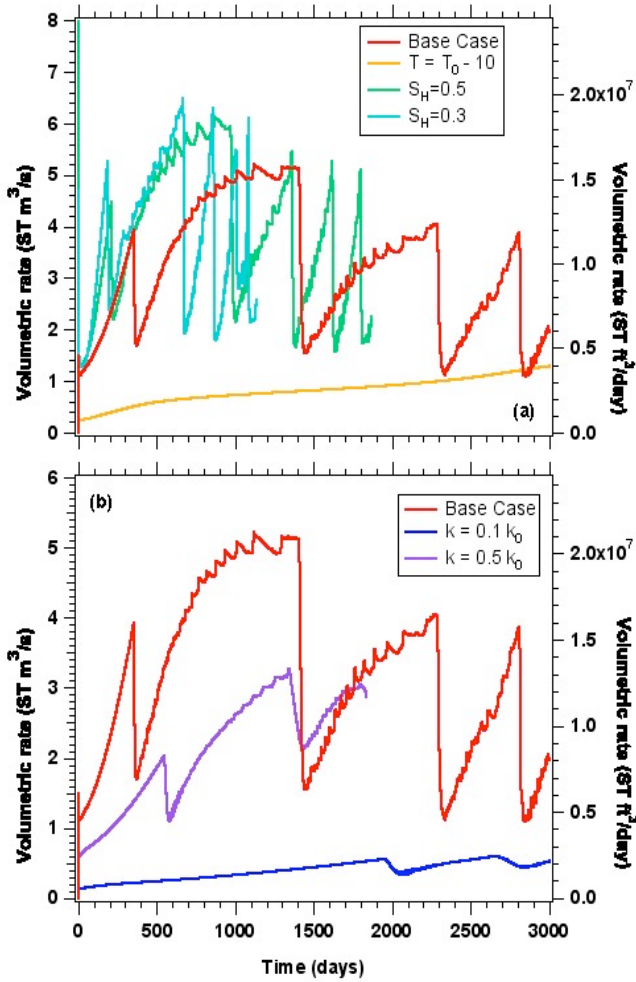
Figure 27 – Sensitivity analysis: effect of various perturbation parameters on Q_P during production from the Class 3 oceanic hydrate deposit in Case C.
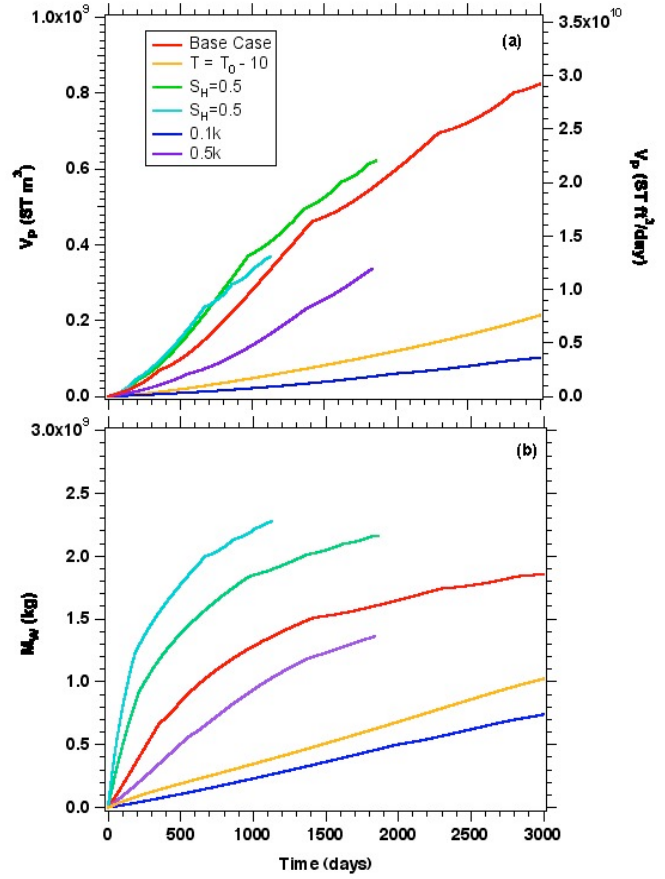
Figure 28 – Sensitivity analysis: effect of various perturbation parameters on V_P and M_W during production from the Class 3 oceanic hydrate deposit in Case C.
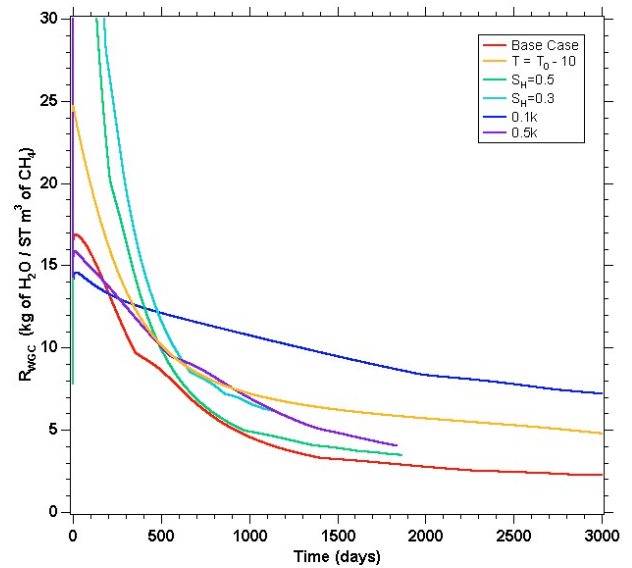

Figure 29 – Sensitivity analysis: effect of various perturbation parameters on the evolution of the cumulative water-to-gas ratio R_{WGC} during production from the Class 3 oceanic hydrate deposit in Case C.
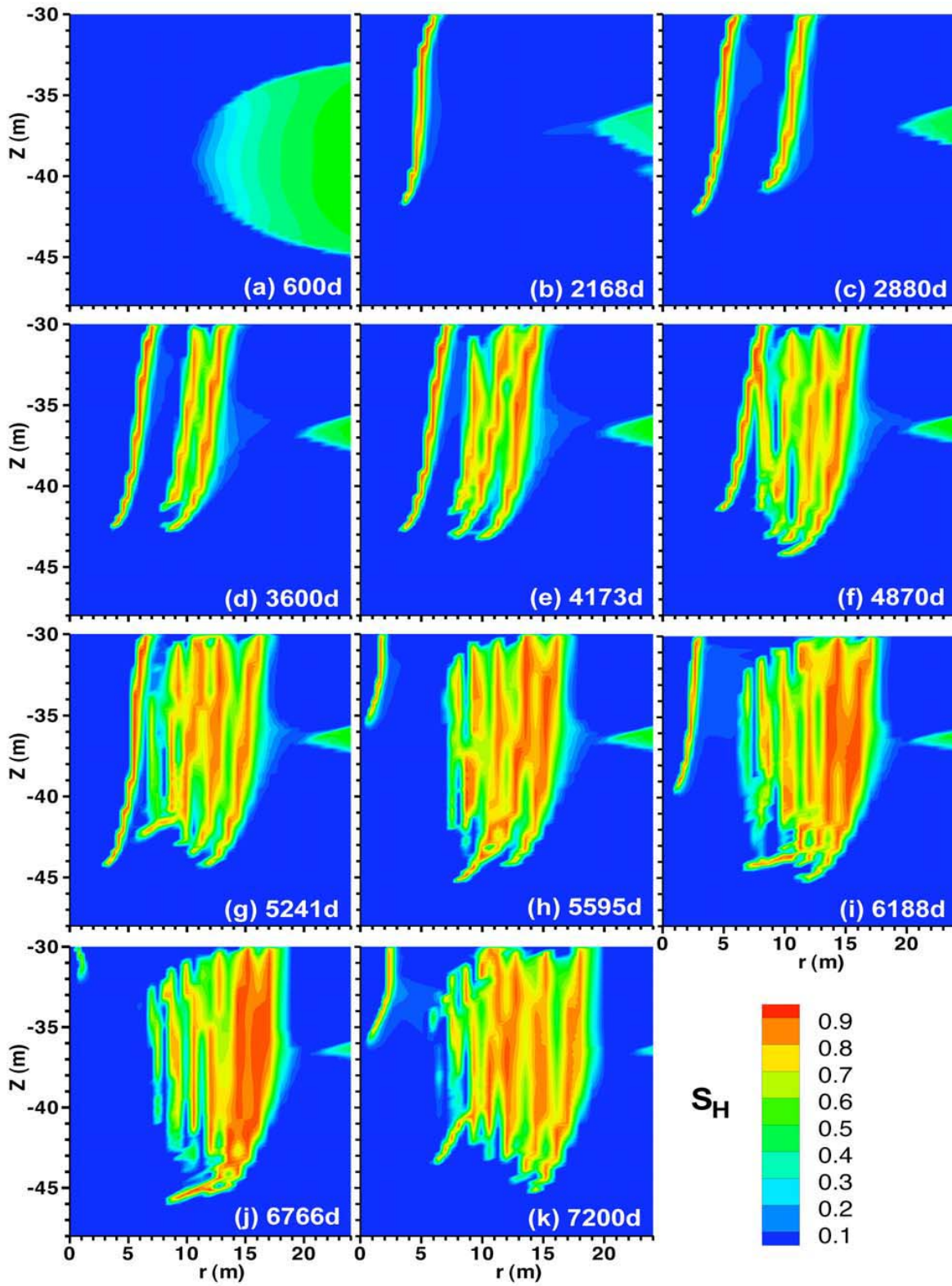
Figure 30 –Evolution of spatial distribution of S$_H$ during gas production from a Class 3 oceanic hydrate deposit in Case C with *k* = 0.1*k$_{ref}$*.
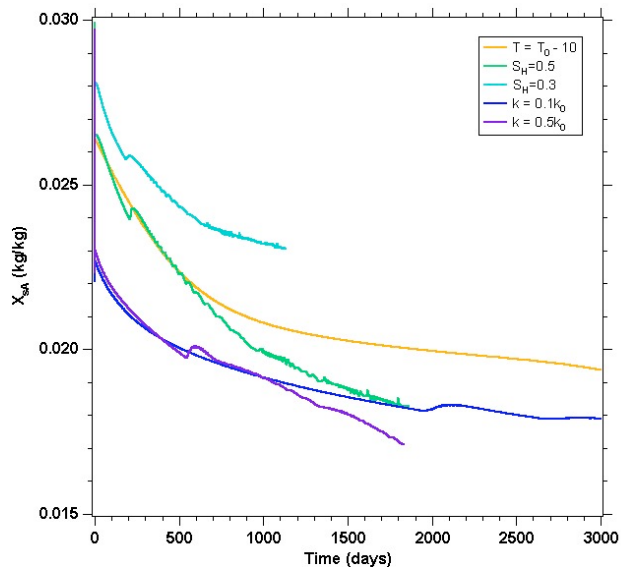
Figure 31 – Evolution of the salinity in the water produced at the well during production from the Class 3 oceanic hydrate deposit in Case C. The effect of various perturbation parameters is depicted.